journal of the international meteor organization

WGN

49:5
october 2021

Sporadic E in Europe during May to August, 2021

IMC 2021 special issue:

ISSN 1016-3115

WGN Vol. 49, No. 5, October 2021, pp. 113 – 144

Administrative

Radio Meteors

Conferences

Front cover photo

Bright fireball captured by the Allsky7 camera AMS77 on 2021 November 8, at $22^{\mathrm{h}}37^{\mathrm{m}}01^{\mathrm{s}}$ UT from Rezman Observatory, Slovenia. Image courtesy: Javor Kac and Yves Bastian / Allsky7.net

Writing for WGN

This Journal welcomes papers submitted for publication. All papers are reviewed for scientific content, and edited for English and style. Instructions for authors can be found in WGN **45:1**, 1–5, and at `http://www.imo.net/docs/writingforwgn.pdf` .

Legal address

International Meteor Organization, Jozef Mattheessensstraat 60, 2540 Hove, Belgium.

From the Treasurer — IMO Membership/WGN Subscription Renewal for 2022

Marc Gyssens

Renewal rates

Most members/subscribers whose membership/subscription has expired should have received a reminder email by the time you receive this issue of WGN. Via this way, we invite them again to renew for 2022.

The fees are as tabulated below. We are happy that we can offer WGN at the same cost as last year. We also continue to offer an electronic-only subscription at a reduced rate.

IMO Membership/WGN Subscription 2022				
Electronic + paper with surface mail delivery:		€26		US$ 32
Electronic + paper with airmail delivery (outside Europe only):		€49		US$ 60
Electronic only:		€21		US$ 25
Supporting membership:	add	€26	add	US$ 32

It is also possible to renew for two or more years in a row.

When you renew, give a few minutes of thought to becoming a **supporting member** by paying at least 26 EUR/32 USD extra. Smaller gifts are of course also appreciated. As you may know, there is an IMO Support Fund. With this Support Fund, we offer support to meteor-related projects. Our ability to provide this service to the meteor community depends primarily on the gifts we receive from supporting members!

Another way to help meteor workers with limited funds is to offer them a gift subscription.

We already thank all our members that will renew for their continued trust in our Organization!

Payment instructions

You first must log in into your account at the IMO website if you want to renew. For this purpose, click the log-in button in the upper right-hand corner. As login, use the email address on which you received my reminder email. In case you forgot your password, you can use the "forgot password" link to reset it. Once logged in, you will see your profile picture (or the space provided for it). If you read on the green button below it that your membership is about to expire, click it, and the rest will be self-explanatory.[1]

The outcome of this process is that you will see the total amount due and your payment options. If you choose to pay using PayPal (or using a credit card via PayPal), you can complete the payment on our website.

If you experience any difficulties, do not hesitate to contact me at `treasurer@imo.net`.

One final request: every year, a lot of members renew late. As a consequence, back issues that already appeared have to be sent out to these members. Please support our volunteers in their bimonthly effort to have WGN shipped to you by renewing promptly! Thank you for your understanding and cooperation!

[1] Alternatively, you can also click on "Extend your membership" in the pull-down menu to the right of your name in the upper right-hand corner, with the same result.

Radio Meteors

Study of Sporadic E Occurrence in Europe 2021

Wolfgang Kaufmann[1]

The formation of sporadic E layers (Es) over Europe was studied by means of a simple amateur radio station during May to August, 2021. Diurnal solar tides as well as the lunar tide could be clearly identified. Geographical hot spots of preferred Es occurrence were recognized. The reflected radio power showed a distinct Weibull distribution being responsible for a couple of extraordinary high free electron density Es events. The measuring campaign failed to identify a relationship between solar wind induced geomagnetic disturbances and the forming of Es. Also the influence of major meteor showers could not be demonstrated unambiguously.

Received 2021 July 19

1 Introduction

The term "Sporadic E" (Es) is used for the thin layers of enhanced metallic ionization that form in the E region ionosphere, mostly between about 95 and 120 km. The formation of Es is inextricably linked to meteoroids entering Earth's atmosphere. Not only the phenomenon itself is worth a study but in terms of radio meteor observation Es also can bias or hamper the recording of meteors. It can produce false positives or suppress the detection of radio reflections off meteors. Hence the study of the Es formation has a practical benefit also. The aim of this paper is to describe the radio observable forming of sporadic E layers (Es) by means of an amateur radio station in the light of scientific insight.

Sporadic E layers can at times become denser than the normal E layer and therefore are an important phenomenon in radio wave propagation up to 150 MHz. Therefore even radio forward scattering observation with the French GRAVES-radar can be affected. The Es occurrence underlies a strong geographical, seasonal and diurnal variation. A comprehensive review gives Haldoupis (2011).

The physics of the mid-latitude sporadic E layer formation is described through the *Windshear Theory*, first proposed and formulated in the early sixties by Whitehead (1961), and Axford (1963). Accordingly the central forces of the forming process of Es are the Earth's magnetic field, the metallic ion concentration and wind shears in horizontal neutral winds in the mesosphere/lower thermosphere (MLT, corresponding to the ionospheric E region). In the middle atmosphere exist stacked reverse wind flows as zonal as well as meridional wind fields. Between such two reverse horizontal wind flows there exists a layer with a wind shear velocity of null. In case of a westward wind above and an eastward wind below metallic ions in the wind flows are Lorentz-forced by the horizontal component of the magnetic field to drift downwards (upwards) and aggregate in the wind shear null zone. In case of a northward wind above and a southward wind below (in the northern hemisphere) the ions are constrained by the Lorentz force to gyrate about the inclined magnetic field lines. As a result, the ions finally move in the direction of the magnetic field and therefore converge to the wind shear null to form a layer. Free electrons are then attracted by the positive charge of the compressed ions and move along the magnetic field lines to neutralize this charge (Whitehead, 1997). The resulting high densities of free electrons are responsible for the refraction of radio waves. For the formation of Es-layers zonal winds are significantly more effective than meridional winds.

Vincent (2015) describes the MLT wind dynamics as follows: Zonal mean winds are reaching peak values of approximately 60 to 70 ms−1 near 70 km and then they reduce in magnitude until they reverse sign at heights between 90 and 100 km. These mean winds are superimposed by planetary waves, atmospheric solar tides and gravity waves. The source regions for all these waves are lower in the atmosphere. As the waves propagate upward their amplitudes grow exponentially to compensate for the decrease in atmospheric density. Consequently, these wave motions often dominate the wind field in the MLT. Especially the atmospheric solar tides with wave periods of a solar day and its sub-harmonics substantially affect the mean MLT-wind flows (Fytterer et al., 2013). They are named diurnal tide (DT, period 24 h), semidiurnal tide (SDT, period 12 h) and terdiurnal tide (TDT, period 8 h) and are responsible for the characteristic diurnal bimodal Es intensity progression.

The metallic ion concentration also is an essential constituent in Es layer forming. Metallic ions have lifetimes from a few days at $\sim$ 120 km to a few hours at $\sim$ 95 km height (MacDougall et al., 2000). Only these persistent ions are able to build up Es layers existing from a few to many hours. These ions originate from incoming meteoroids. The seasonal and geographical variation of the meteoric influx is thought to be responsible for Es occurrence and intensity which is marked by a conspicuous maximum during June–July and a minor peak during December for the northern hemisphere (e.g. Basu et al., 1974). Figure 1 shows the daily meteor counts over middle Europe received by Felix Verbelen at Kampenhout, Belgium, 2020 (personal communication). We find a clear maximum in June/July and a smaller second increase in December.

[1]Lindenweg 1e, 31191 Algermissen, Germany. Email: contact@ars-electromagentica.de.

IMO bibcode WGN-495-kaufmann-sporadice
NASA-ADS bibcode 2021JIMO...49..114K

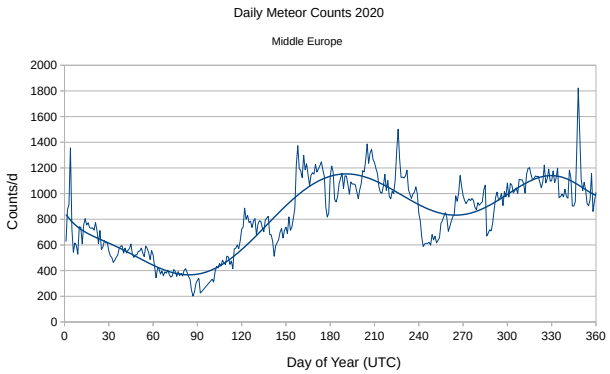

Figure 1 – Daily meteor counts in 2020, recorded in Kampenhout, Belgium, by F. Verbelen using a 2 element Yagi pointing, with an elevation of 52°, to a beacon located near Ieper – distance some 120 km. The beacon is a 2 element crossed yagi pointing to the zenith and beaming a power of 50 Watts (CW) on 49.99 MHz. Data by courtesy of F. Verbelen.

The third important constituent in Es layer forming is the strength of the horizontal field component of magnetic field. It is the key agent responsible for the global Es occurrence distribution. At the two mid-latitude regions of the globe where the horizontal magnetic field is strongly reduced we find the corresponding deep minima in the Es occurrence: one over the south Atlantic in the southern hemisphere and the other over northern America in the northern hemisphere (Arras et. al., 2008).

In this study a CB radio station in the 11 m band was used as hf-beacon as well as receiver. During the minimum of the solar cycle no ionospheric propagation other than via Es will happen. Using the 11 m band enhances the detectability of Es because the amount of radio power being reflected rises with reduced frequency. At least operating a CB-radio is license-free. The digital weak signal mode JS8 is employed. The related en-/decoding software has an automatic reporting function which allows to retrieve reception reports of the own beacon signal all over the world through an internet-accessible database. The logarithmic signal to noise ratio, time and location (given as Maidenhead Grid Locator) of each successful reception are part of these reports. So a pan-European net of CB-radio stations in JS8 mode can be used to observe the occurrence of Es. The number of reports per time unit shall act as a measure of Es occurrence.

2 Material and Methods

The 11 m CB-radio station was situated in Algermissen, Northern Germany (Maidenhead locator JO42XG, callsign 13WKA5). A President McKinley transceiver in USB-mode was employed. It was connected to a $\lambda/4$-ground-plane antenna (Sirio Signalkeeper) which was mounted 1 m above ground. A computer was connected via a SignaLink USB-Interface to the microphone-jack of the transceiver. Digital weak signal mode JS8 (JS8Call v2.2.0 by KN4CRD) was used to transmit heartbeats in normal speed every 6 minutes regularly between 5 and 20 hours UTC. Former observations with this setup revealed that detecting Es occurrence was largely limited to this time span. However, this period was extended to 24 h in case of the very rare longer lasting propagation conditions. The transceiver was tuned to the international data mode channel 25 (27.245 MHz), the output power was set to 6 W. JS8Call automatically reports all receptions to PSK-reporter[a]. This database was used to get weekly logs of all stations that received 13WKA5 and were received by 13WKA5.

Statistical calculations and plots are done with "PAST" v4.0, Hammer et al. (2001) and the "Free Statistics and Forecasting Software", Wessa (2021).

The measurements were performed in 2021 from May 1st to August 31th. The solar cycle no. 25 was in its early beginning. Therefore, the solar sun spot number was low and the maximal usable frequency never reached the 11 m band. All propagated signals in the 11 m band were due to Es (any reports from stations via direct or ground wave are excluded).

3 Results

The amount of refraction of radio waves that occurs at the Es layer depends on three main factors:

1. the density of free electrons (depending on the metallic ion density),
2. the frequency of the radio wave, and
3. the angle at which the radio waves enters the layer.

In this setup the frequency is fixed. For a given receiving station the angle is also fixed. The radio power received at this station then only depends on the transmitted power and the free electron density in the Es-layer.

Table 1 gives an overview about the number of received reports from European radio stations having decoded successfully JS8-transmissions from 13WKA5 (group 1, G1) as well as reports about stations heard by 13WKA5 (group 2, G2). June and July were the months with the highest number of reports and were used for a couple of analyses. The consistently higher number of G2 reports resulted from stations with a higher HF-output power than the 6 W of the 13WKA5 CB radio station. The higher HF-output compensated for lower free electron densities in the Es-layer resulting in a higher detectability of these stations. For consistent results only the G1-reports were used in the analyses. They are based on constant output-power, constant on-air times and scheduled continuous transmissions of the 13WKA5 CB-station.

The reporting stations were spread all over Europe. Figure 2 shows each station within an azimuthal map centred on the transmitting site in Northern Germany. There are some gaps: the section between 300°–0° covers mostly the North sea and the section between 60°–120° seems to be sparsely populated with JS8-stations.

[a] `https://www.pskreporter.info/pskmap.html`

Table 1 – Monthly number of Es related reports 2021. Group 1: number of reports from stations hearing 13WKA5. Group 2: number of stations heard by 13WKA5.

Group Nr.	May	June	July	August
1	637	1563	1735	814
2	1166	2416	2586	1278

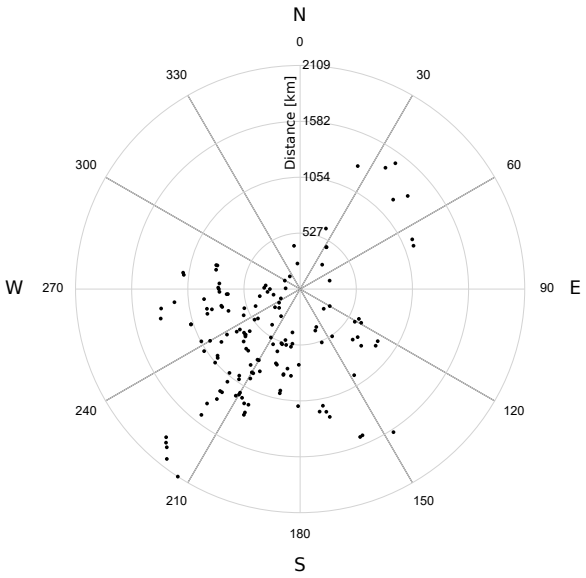

Figure 2 – Azimuthal map of all stations that gave a reception report during the measuring period. The map is centred on the site of the CB radio station 13WKA5 near Hildesheim, Northern Germany.

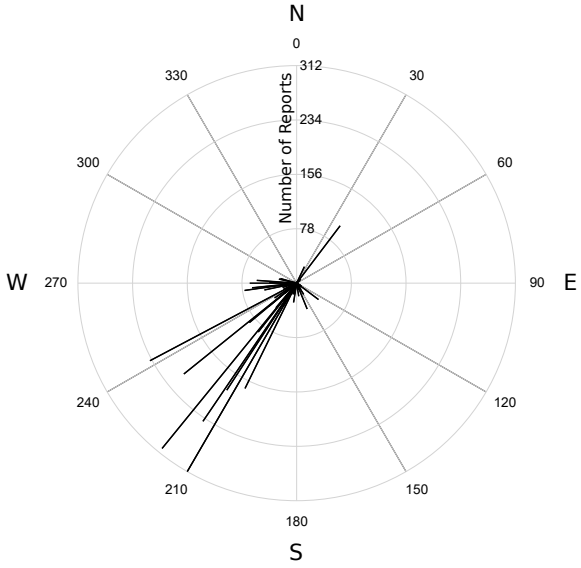

Figure 3 – Azimuthal map of the reporting frequency of radio stations in June/July as length of spokes. The map is centred on the site of the CB radio station 13WKA5 near Hildesheim, Northern Germany.

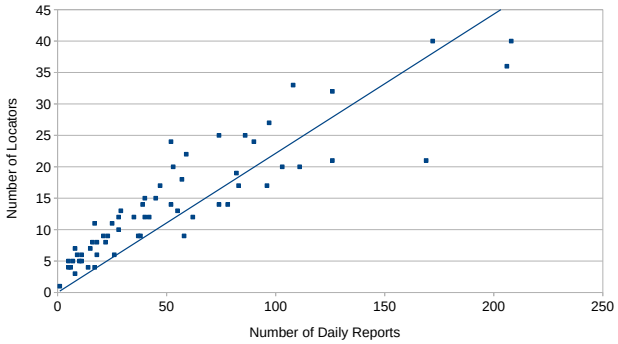

Figure 4 – Number of daily reports from pan-European radio stations in June/July plotted against the number of different locators of reception. A linear function with a correlation coefficient of 0.9 fits the data.

The number of reported receptions from the single stations were very different. There existed propagations paths that were open almost every day in the June/July-period. On the other hand there were stations, that reported only a small number of receptions. An azimuthal map illustrates the findings showing the number of reports as length of spokes, see Figure 3. Apparently in south-west direction (France, Spain, Portugal) the occurrence of Es was highest followed by north-western directions (southern Sweden, Finland) and last western directions (Ireland, UK). Some bias must be expected by radio stations that are only intermittently on air (e.g. at times of good DX-conditions) thereby missing short Es events.

The graph in Figure 3 could imply that the overall number of reports only resulted from the reporting of a few recurring stations and therefore were not suited as a measure of Es occurrence in general. Hence the number of daily reports were plotted against the number of different locators where the transmissions were received, see Figure 4. The graph reveals a linear relationship with a positive slope. This means the prominent propagation paths in Figure 3 were always part of a set of broadly distributed reception locators.

The distribution of the received logarithmic signal to noise ratio (SNR) of the transmitted signal is depicted in Figure 5. The SNR-span reaches from −24 dB to +15 dB. Thereby, a SNR of −24 dB is the lower threshold for a successful JS8 decoding according to the developer of the JS8-mode. The distribution is characterized by a fast rise of reports and a slower decline of reports with increasing SNR. It is best fitted by a Weibull-distribution (shape 2.49, scale 17.5, correlation coefficient 0.99). The elongated tail of the distribution towards higher SNR documents a disproportional higher amount of high free electron density events in the Es-layer compared to a normal distribution.

The daily variation of the SNR per propagation path was found to be very high. Figure 6 shows the progression of the SNR of the transmitted signal during one day received by a French station. This example is typical in its high spread of the SNR within short periods of time and reflects the high dynamics in the MLT. This strong diurnal variability makes the SNR inappropriate for the measurement of Es occurrence rates.

The daily distribution of the number of reports shows a distinct diurnal pattern, see Figure 7. It was

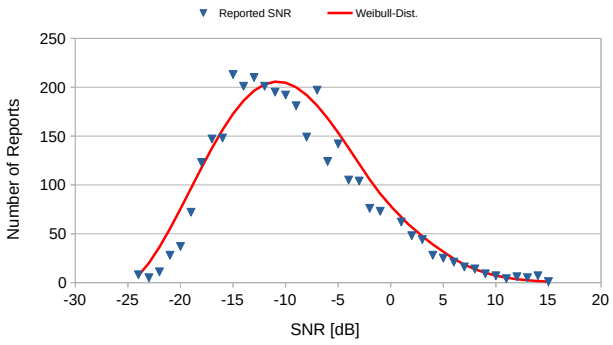

Figure 5 – Frequency distribution of the SNR reported during June/July. A Weibull distribution best fits to the data.

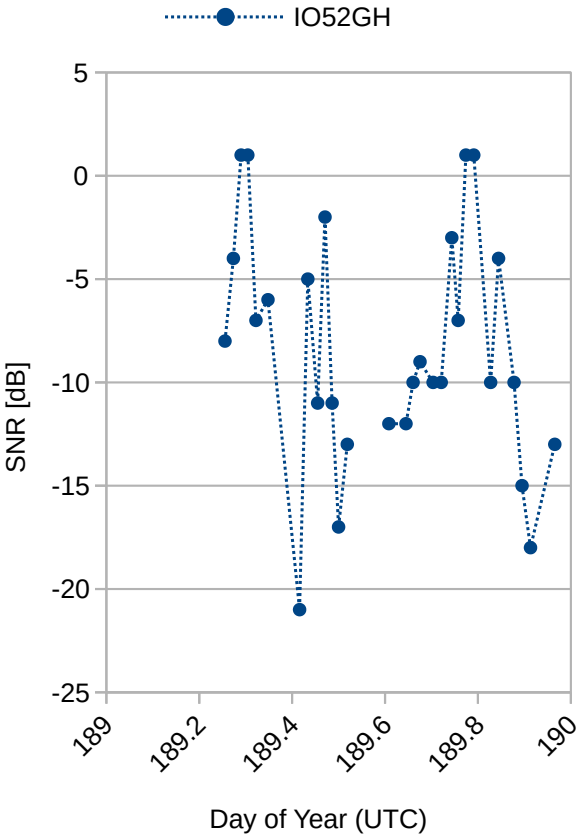

Figure 6 – Variation of the SNR of transmissions from 13WKA5 received by a station in France (Locator IO52GH) on July 8th 2021 UTC.

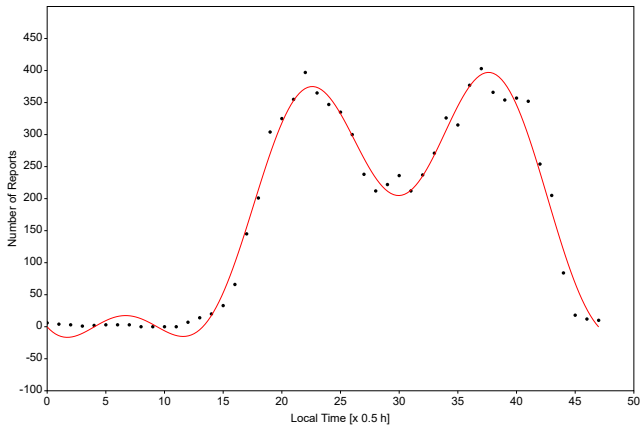

Figure 7 – Total number of reports per half hour local time from June/July. In this analysis the G1- and exceptionally the G2-data were used together to enhance the number of reports to achieve a high correlation coefficient of the sinusoidal fit of 0.98 (The G1-data revealed nearly the same fitting parameters but with a somewhat lower correlation coefficient). Local time is given as CEST.

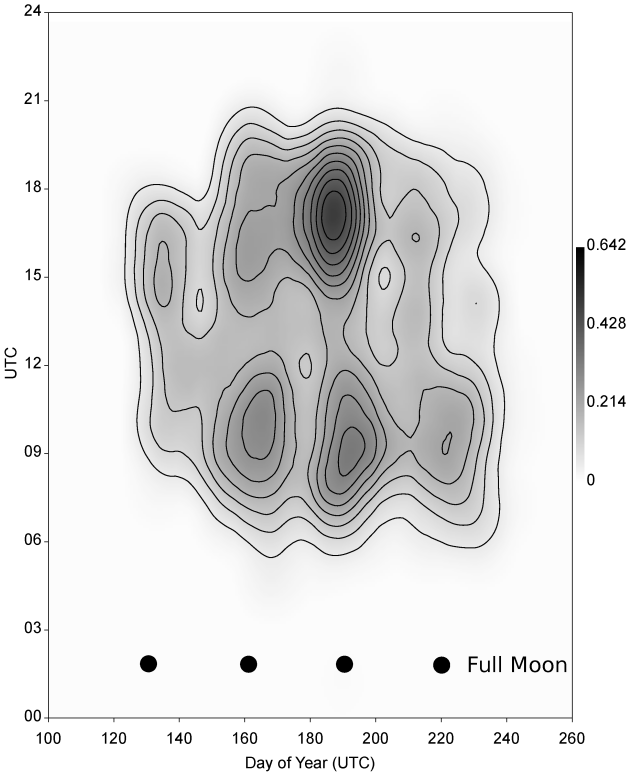

Figure 8 – Contour map of all reports ordered by UTC and day, smoothed by a triangular kernel function (radius = 12.5). The report-density is grey-scale coded. The recording period is May to August. The dates of full moon are indicated.

best fitted with three sinusoids of periods (relative amplitudes) of 23.5 h (1.0), 11.75 h (0.37) and 7.84 h (0.48). This corresponds very well with the periods of the atmospheric solar tides DT, SDT and TDT. It confirms the suitability of the number of reception-reports as a measure of the occurrence rate of Es in principle.

Now we will look at larger scale oscillations of the daily Es occurrence. Figure 8 shows a contour map with the report-density for the period May to August smoothed by a triangular kernel function. The above described diurnal oscillation can be seen well. Interestingly the two daily maxima show differing amplitudes with time. Whereas the Es occurrence in the early evening dominated in May and July the situation changed in June and August where the Es occurrence dominated in the late morning. Another striking feature is the overall oscillation of the Es occurrence showing periodic maxima coinciding with full moon. A sinusoidal fit revealed a period of 28.83 d which is very close to the 29.53 d of the synodic lunar month.

At least a possible influence of disturbances of the horizontal component of Earth's magnetic field (Ap-

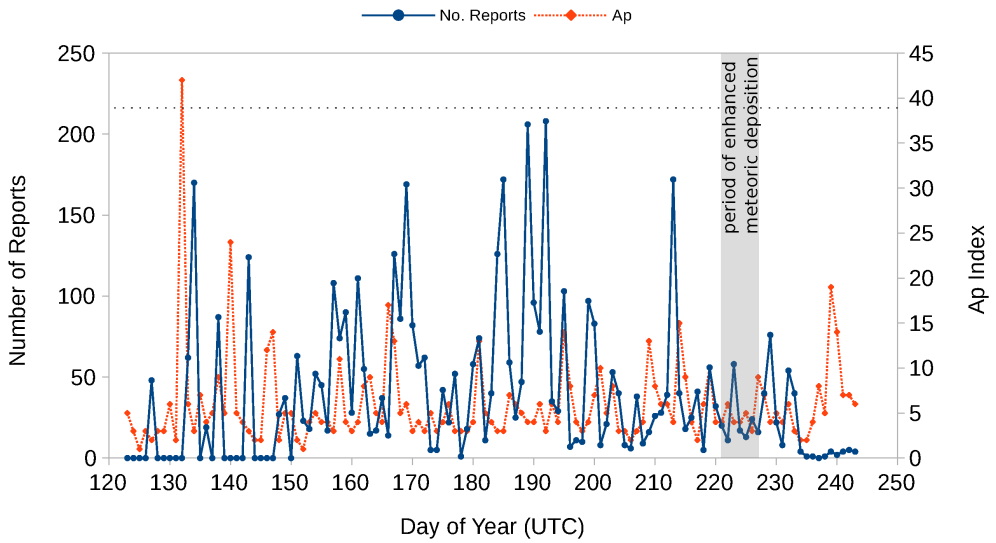

Figure 9 – Number of daily reports in the period May to August and the daily planetary Ap index. The time span of the Perseids as major shower is indicated.

index) and the additional metallic ion deposition from strong meteor showers was considered. Figure 9 shows the daily reports and the planetary Ap index (Matzka et al., 2021). According to NOAA space weather scale[b] a minor geomagnetic storm starts at an Ap-index of 39. Assuming that any influence below this threshold is buried in the highly dynamical processes in the MLT there was only one event at day 132 that exceeds this threshold. At this day no reception was recorded. However, from this single event no general statement can be made.

The same is true with respect to the meteoric influence. Only a strong longer lasting meteor shower may produce a noticeable effect. In the observation period the Perseids was the most prominent meteor shower. It is regarded a major shower in the period August 9th to 15th (gray area in Figure 9) with a maximum zenithal hourly rate (ZHR) of about 100 on August 12th (Rendtel 2014). In this year an additional short but very strong outburst on August 14th between 6 h and 12 h UTC was observed with an ZHR of 210 (Jenniskens & Miskotte, 2021). Looking at Figure 9 the period of enhanced metallic ion deposition may have manifested in a slightly higher number of reports on days 228/229 (August 16th/17th) compared to the previous days. But again from this single observation no general statement can be made.

4 Discussion

The results of the measuring campaign correspond well with the findings of ionospheric and climatological research.

1. After considerable averaging the solar and lunar tides clearly could be identified in Es forming (Figures 7, 8). Whereas the solar tides are diurnal atmospheric oscillations caused by the local solar heating of the Earth the roughly monthly lunar tides are understood as a consequence of the gravitational pull of the Moon (Thurman, 1994).

2. Without averaging the Es free electron density is highly variable within minutes to days (Figures 6, 9). It reflects the high dynamical processes in the MLT e.g. driven by shorter scale gravity waves as well as Kelvin-Helmholtz instabilities. Also plasma instabilities have to be regarded.

3. The Es forming is not a uniform process over Europe but there exist preferred locations with a higher than average Es occurrence rate (Figure 4). Locally favoured formation of wind field patterns in the MLT and/or localised electrodynamic processes may be the reason for this.

4. Also the occurrence of highly ionised Es-layers (reflecting radio waves up 150 MHz) is higher than a normal distribution would predict (Figure 5). The noticed Weibull shape often describes a natural wind speed distribution[c]. This could be the reason for the asymmetric occurrence of high free electron density events.

5. The seasonal occurrence of Es is a well known phenomenon that has not been documented here. It is thought that it is a consequence of the seasonal differing overall meteoric deposition of metallic ions. This is in accordance with the measured daily number of meteors over Middle Europe (Figure 1).

A correlation between the Es forming and the disturbance of the geomagnetic field by coronal mass ejections (geomagnetic storms) could not be established because of low number of observations. Also the influence of enhanced short term meteoric metallic ion deposition could not be ascertained. A higher number of observations would be necessary to reliably filter out these effects if they exist anyway.

[b] https://www.swpc.noaa.gov/noaa-scales-explanation

[c] http://www.reuk.co.uk/wordpress/wind/wind-speed-distribution-weibull/

5 Conclusion

The main determinants of observed Es occurrence can be uncovered by means of a radio amateur. However, only when sophisticated methods and techniques became available, scientific studies could reveal the mechanisms that were able to explain these observations. The "mystery" of Es is much cleared up nowadays but its stochastic behaviour remains. Its occurrence is a question of probability as it is with all complex systems.

Acknowledgement

The author thanks Felix Verbelen for sharing his radio meteor observation data. This data was highly welcomed, due to the fact it was consistently recorded in the Middle Europe. The author also thanks James DuCharme for double-checking the draft and Jean-Louis Rault for giving valuable advice in his review.

References

Arras C., Wickert J., Beyerle G., Heise S., Schmidt T., and Jacobi C. (2008). "A global climatology of ionospheric irregularities derived from GPS radio occultation". *Geophys Res Lett*, **35:14**, L14809.

Axford W. I. (1963). "The formation and vertical movement of dense ionized layers in the ionosphere". *J Geophys Res*, **68:3**, 769–779.

Basu S., Vesprini R. L., and Aarons J. (1974). "Study of field-aligned ionospheric E-Region irregularities & sporadic E at hf". *Indian Journal of Radio & Space Physics*, **3**, 70–75.

Fytterer T., Arras C., and Jacobi C. (2013). "Terdiurnal signatures in sporadic E layers at midlatitudes". *Adv. Radio Sci.*, **11**, 333–339.

Haldoupis C. (2011). "A tutorial review on sporadic E layers". In Abdu M. A., Pancheva D., and Bhattacharyya A., editors, *Aeronomy of the Earth's Atmosphere and Ionosphere*. Springer Science+Business Media B.V., pages 381–394.

Hammer Ã., Harper D. A. T., and Ryan P. D. (2001). "PAST: Paleontological statistics software package for education and data analysis". *Palaeontologia Electronica*, **4:1**, 9.

Jenniskens P. and Miskotte K. (2021). "Perseid outburst 2021". *eMeteorNews*, **6**, 460–461.

MacDougall J. W., Plane J. M., and Jayachandran P. T. (2000). "Polar cap Sporadic E: part 2, modeling". *J Atmos Solar-Terr Phys*, **62:13**, 1169–1176.

Matzka J., Stolle C., Yamazaki Y., Bronkalla O., and Morschhauser A. (2021). "The geomagnetic Kp index and derived indices of geomagnetic activity". *Space Weather*, **19:5**. `https://doi.org/10.1029/2020SW002641`.

Rendtel J., editor (2014). *Meteor Shower Workbook 2014*. International Meteor Organisation, Potsdam.

Thurman H. V. (1994). *Introductory Oceanography, 7th.* Macmillan, New York.

Vincent R. A. (2015). "The dynamics of the mesosphere and lower thermosphere: a brief review". *Progress in Earth and Planetary Science*, **2**, 4.

Wessa P. (2021). "Free Statistics Software, Office for Research Development and Education, version 1.2.1". `https://www.wessa.net/` .

Whitehead D. (1997). "Sporadic E–A Mystery Solved? Part 2". *QST November 1997*, pages 38–42.

Whitehead J. D. (1961). "The formation of the sporadic E layer in the temperate zones". *J Atmos Solar-Terr Phys*, **20:1**, 49–58.

Handling Editor: Jean-Louis Rault

Conferences

Calibration of visual meteor observations

Jürgen Rendtel[1], *Ralf Koschack*[2]

Corrections for the limiting magnitude lead to systematic underestimations of the ZHR for shower returns observed in moonlit skies. Here we describe attempts to improve the limiting magnitude correction factor as well as possibilities to derive the ZHR from other methods. Dedicated observations to provide data for both the calibration of the ZHR and to improve the limiting magnitude correction by including the background illumination are recommended. A good opportunity for a ZHR calibration period is expected during the Geminid maximum in 2021.

Received 2021 October 21

This work has been presented at the International Meteor Conference 2021 (held online).

1 Introduction

The procedures of visual meteor observations have been established before 1990 and have been described in detail in the IMO's Meteor Observers Handbook (Rendtel & Arlt, 2014). Results have been obtained for many showers. For an overview see, e.g. Koten et al. (2019). The general recommendation is to observe under dark skies and to omit periods with bright background (twilight, moonlight, artificial light etc.). However, there are several occasions where observational data is of high interest – poor conditions or not. Among these are outbursts, major shower maxima connected with dust trail or filament encounters, or activity from sources which can only be observed in twilight (daytime showers).

Usually, activity profiles show gaps with no observations and often we have no information about a shower's maximum (Figure 1). Another effect we found at several occasions is an obvious underestimation of the rate when data around Full Moon have been calculated. An example is the Perseid "pair" of 1989 and 1990 (Figure 2) – both returns with no exceptional high ZHR and well before the series of intense returns in the 1990-ies. While the "moonless" 1989 peak ZHR was well above 100, the "moonlit" 1990 peak values are of the order of 80 (and the profile is composed of fewer values).

Observers repeatedly comment that they still see faint stars but not the corresponding meteors when the sky background is illuminated. We try to explain this effect and propose a series of observations which may shed light into the case.

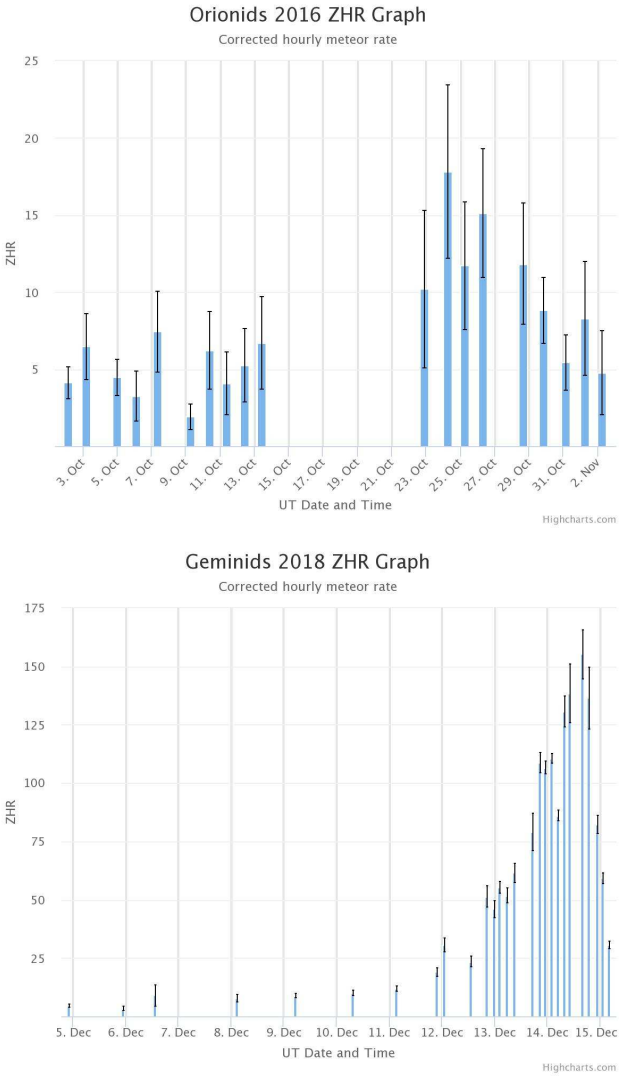

Figure 1 – Live graphs of the 2016 Orionids and the 2018 Geminids interrupted or stopped by the Full Moon period. For such returns we have either no or much limited information about the shower (both in terms of the population index and the ZHR).

2 The meteor limiting magnitude

The *stellar* limiting magnitude is determined from star counts in pre-defined fields (described in detail in the IMO Handbook for Meteor Observers – see Rendtel & Arlt, 2014). This should represent the *limiting magnitude for meteors* close to the line of sight, with a dependence on the angular velocity of the meteors. Additionally, the observer's perception further affects

[1]International Meteor Organization, Eschenweg 16, 14476 Potsdam, Germany. Email: jrendtel@web.de
[2]International Meteor Organization, Hauptstraße 35, 18469 Velgast, Germany. Email: ralf.koschack@meteoros.de

IMO bibcode WGN-495-rendtel-calibration
NASA-ADS bibcode 2021JIMO...49..120R

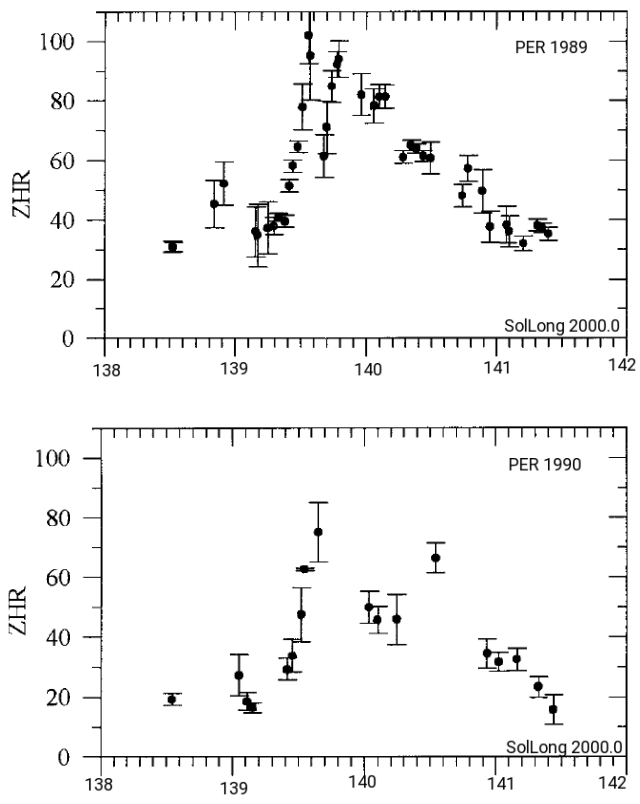

Figure 2 – Although the Perseid profiles of 1989 and 1990 seem to be complete, the moonlight interference in 1990 (Full Moon on August 6) resulted in fewer reports and larger error margins. Especially, the much lower peak ZHR is obvious (ZHR profiles from Brown and Rendtel (1996)).

the personal meteor limiting magnitude. One implicit assumption is that a reduction of the *stellar* limiting magnitude happens in the same way as the reduction of the *meteor* limiting magnitude, and that reduction near the centre of the field of view happens in the same way as in some distance from the centre. This seems to work if the transparency (transmission) of the sky varies. This may be treated like a neutral grey filter which absorbs uniformly and does not affect the signal-to-noise ratio.

Certainly, the *meteor* limiting magnitude depends on the brightness, angular velocity and obviously on the sky background brightness. The angular velocity affects the "integration time" (how many photons reach a receptor in the eye). A rough estimation indicates that a fast meteor (30°/s) has to be about 2 magnitude brighter than a slow meteor (5°/s) to produce the same receptor effect. This, for example, strongly affects observations of meteors of a shower with high velocity and the radiant low in the sky: then all meteors appearing high in the sky have high angular velocities while a field centre below 50° elevation implies an obstruction. This was the case e.g. during the Aurigid outburst in 2021 (Rendtel & Koschack, 2021).

We may roughly estimate the situation. A meteor usually lasts longer than the human eye integration time (which is probably between 0.04 s and 0.2 s), so we get the full amount of light per receptor. For a limiting magnitude of +6.5, the corresponding brightness from a sky quality meter (SQM) is +21.5 for a square arc second of the sky (Crumey, 2014). Assuming a signal-to-noise ratio of about 5 for the detection results in a difference of $2.5 \times \log(5) \approx 1.7$ to the background magnitude. The latter value probably depends on the personal perception.

Any background brightness badly affects the contrast. A visual observer witnesses faint meteors only close to the line of sight, while brighter ones can also be seen at larger distances. Hence, the fainter meteors – close to the detection threshold – are "lost" while the brighter ones remain visible, even at some distance to the field centre. The loss of faint meteors is larger for a high population index. Such a loss also affects the value of the population index derived from the meteor sample (expected to tend to a lower value) and the number of meteors. Both effects would act into the same direction (lowered r and ZHR).

3 Observing proposals

Contrary to the general recommendation, we suggest to observe visually also during periods with moonlight interference. There are several ways to derive information about the validity of the applied corrections.

We may use periods which leave some geographical regions moon-free while others are in moonlight. This may work for showers with the radiant well above the horizon for a long portion of the night so that there is enough overlap. The Geminid maximum in 2021 is an excellent occasion as the Moon sets around 2^{h} local time leaving a part of the second half of the night undisturbed. The shower can be observed from essentially all locations, we may expect a global coverage and good overlap even over large distances. For example, on 2021 December 14 at 5^{h} UT we find dark skies and the Geminid radiant high over Europe. At the same time, observers in North America are before or near local midnight. So the sky is moonlit, but even at 120° W the radiant is high (corresponding to 21^{h} local time). So we may calibrate the data using rates from the same UT period.

Applying the suggested method to derive the rate and the magnitude correction from one data set (Richter, 2021) we may also detect the difference between dark and moonlit skies. Note that the magnitude correction q here is not the same as the population index r, which is a physical quantity of a shower, caused by the (true) number of meteors over a magnitude range.

We also may try to apply the method described for the determination of the population index from video data by using data samples obtained under quite different conditions by finding the best fit (Molau et al., 2015).

Recently, we started dedicated observations to analyse the visibility of stars and meteors in dependence on the distance to the field centre. These are different from the series made for the determination of the probabilities of perception (Koschack & Rendtel, 1990) and will be described in a later publication. The aim of this

observations is to review the currently used correction factors.

4 Conclusions

Since all the suggested procedures require a solid sample covering a wide variety of conditions, we call for your participation. Participating observers must carefully record the observing circumstances during visual observations. Apart from the usual interval data (especially the limiting magnitude), we think it is useful to add information about the sky conditions to the session comments. The main information concerns the background illumination, perhaps using the Bortle scale (Bortle, 2001) or, if available, the sky background brightness measured with a sky quality meter (SQM). For this purpose, the interval lengths should not only be adapted to the activity level, it is also important to have separate intervals if conditions change.

The aims of visual meteor observations in moonlit skies are the following:

1. obtaining complete activity profiles of shower (maxima);
2. deriving reliable peak data for events occurring under poor conditions;
3. improving value of daytime shower data (twilight observations); and
4. determining the effect of sky background illumination quantitatively.

Proposals for upcoming events include the following:

- the Geminid maximum 2021 with roughly half of the night moonlit, which will allow us to use overlapping intervals with/without Moon;
- the Perseids 2022 occurring at Full Moon; here we may apply findings from the first campaign and intermediate results and also test all suggested methods.

References

Bortle J. E. (2001). "Introducing the Bortle Dark-Sky Scale". *Sky and Telescope*, **101:2**, 126.

Brown P. and Rendtel J. (1996). "The Perseid meteoroid stream: characterization of recent activity from visual observations". *Icarus*, **124**, 414–428.

Crumey A. (2014). "Human contrast threshold and astronomical visibility". *MNRAS*, **442**, 2600–2619.

Koschack R. and Rendtel J. (1990). "Determination of spatial number density and mass index from visual meteor observations (I)". *WGN, Journal of the IMO*, **18**, 44–58.

Koten P., Rendtel J., Shrbený L., Gural P. S., Borovička J., and Kozak P. (2019). "Meteors and meteor showers as observed by optical techniques". In Asher D. J., Ryabova G. O., and Campbell-Brown M. D., editors, *Meteoroids: Sources of Meteors on Earth and Beyond*. Cambridge Univ. Press, pages 90–116.

Molau S., Barentsen G., and Crivello S. (2015). "Obtaining population indices from video observations of meteors". In Rault J.-L. and Roggemans P., editors, *Proceedings of the IMC, Giron, France, 18-21 September 2014*. pages 74–80.

Rendtel J. and Arlt R., editors (2014). *Handbook for Meteor Observers*. International Meteor Organization, Potsdam.

Rendtel J. and Koschack R. (2021). "Letter – Aurigid outburst on 2021 August 31". *WGN, Journal of the IMO*, **49**, 73–75.

Richter J. (2021). "Simultaneous estimation of ZHR and the limiting magnitude correction factor". *WGN, Journal of the IMO*, **49**, 35–41.

Handling Editors: Marc Gyssens

This paper has been typeset from a LaTeX file prepared by the authors.

Recent results from the Kilwinning spectroscopic survey for meteors

Bill Ward[1]

Recent results from the Kilwinning Spectroscopic Survey for Meteors are presented. These include spectra from an Ursid meteor, two Quadrantid meteors and a sporadic fireball.

Received 2021 September 25

This work has been presented at the International Meteor Conference 2021 (held online).

1 Introduction

The author has been conducting regular spectroscopic observations from Kilwinning since 2008. These have been mostly made with WATEC 902 or WATEC 910 video cameras.

In order to improve spatial and spectral resolution an ASI ZWO 174MM camera was purchased in 2017. The 174MM is a monochrome camera using the Sony CMOS IMX174LLJ chip with 1936×1216, 5.86 µm pixels. The camera also works at 12 bit resolution which is a improvement on the 8 bit resolution of the frame grabbers currently used with the WATEC cameras. In the camera software the gain is set to 100% and with an exposure of 40 ms. On an i5 processor PC, the camera runs at 17 frames/sec with global shutter, full frame size and max bit depth on USB2.

The camera utilises a $f = 25$ mm, $d/f = 1.3$ Computar CCTV lens designed for 1 inch sensors. In order to maximise wavelength sensitivity, a 600 grooves/mm transmission grating with a fused silica substrate was used as the diffracting element. The fused silica was chosen as it has better UV transmission than normal borosilicate glass. The grating was mounted in a rotating filter holder in front of the lens as shown in Figure 1. A group of four 174MM cameras are now in use.

A selection of recent spectra showing the spectrum quality available given suitably bright meteors are presented.

Figure 1 – General arrangement of the grating mounting.

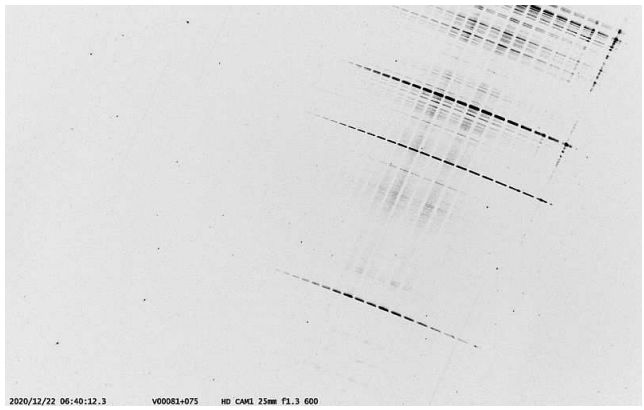

Figure 2 – Ursid spectrum video composite image, recorded on 2020 December 22, $06^{\rm h}40^{\rm m}$ UT.

2 Results

2.1 The Ursids

As a smaller shower the Ursid meteor shower in December is frequently overshadowed by both the much stronger Geminids and poor northern winter weather. However, in 2020 the weather was clear on the night of the peak and several bright Ursids were captured on the various cameras in the array. One camera captured a well placed and well dispersed spectrum.

Due to the fortunate fall of the meteor the wavelength range captured spans ≈ 360nm to ≈ 900nm. This is almost all of the wavelength range that a silicon based sensor is sensitive to. The entire video composite spectrum is shown in Figure 2. The spectrum shows many lines! These are mostly of iron with magnesium, manganese, silicon, sodium and calcium lines. The spectrum graph and colourised synthetic spectrum are shown in Figures 3 and 4.

2.2 The Quadrantids

The examples shown here also had a fortunate fall in the field of view and again the entire spectrum range was captured. However in these examples though, the individual spectrum frames are shown. This is one advantage of the global shutter. Each frame can be viewed in isolation. These spectra show the very strong magnesium lines that are present in the Quadrantid meteor spectra.

The spectra, spectrum graphs and synthetic spectra are show in Figures 5, 6, 7, 8, 9 and 10.

[1]Woodwynd, Kilwinning, North Ayrshire, Scotland, UK. Email: bill_meteor@yahoo.com

IMO bibcode WGN-495-ward-spectroscopic
NASA-ADS bibcode 2021JIMO...49..123W

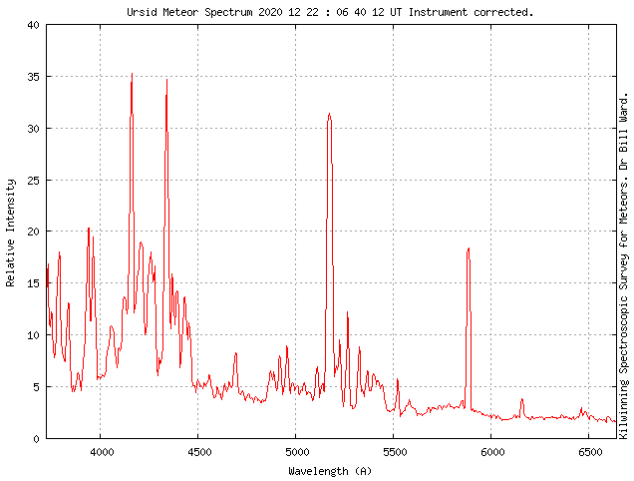

Figure 3 – Corrected Ursid spectrum graph. The main lines here are Ca at 4227 A, Fe at 4384 A, Mg Triplet at 5174 A and Na at 5893 A.

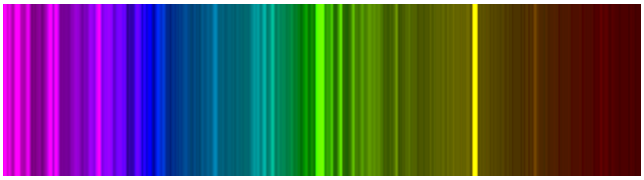

Figure 4 – Synthetic colourised Ursid spectrum.

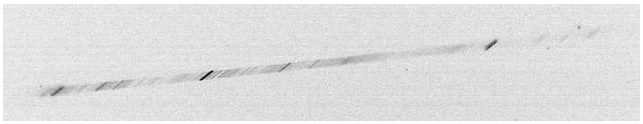

Figure 5 – Quadrantid 1 meteor spectrum image, recorded on 2021 January 03, $05^{h}30^{m}$ UT.

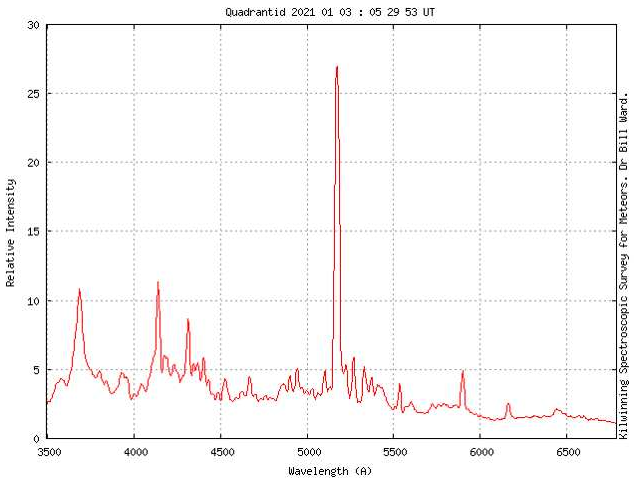

Figure 6 – Quadrantid 1, corrected spectrum graph. The main lines here are Si^{+} at 4131 A, Ca at 4427 A, Mg Triplet at 5174 A and Na at 5893 A.

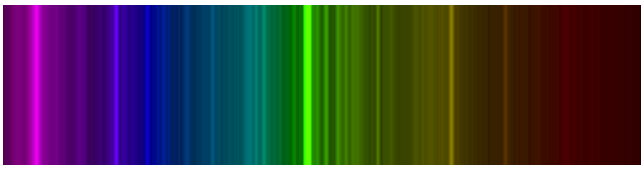

Figure 7 – Quadrantid 1 synthetic colourised spectrum.

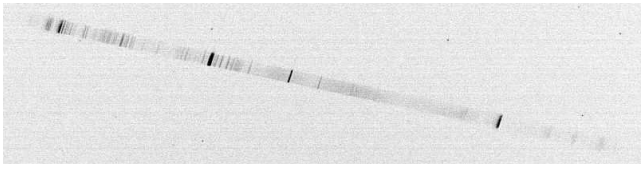

Figure 8 – Quadrantid 2 meteor spectrum image, recorded on 2021 January 03, $06^{h}02^{m}$ UT.

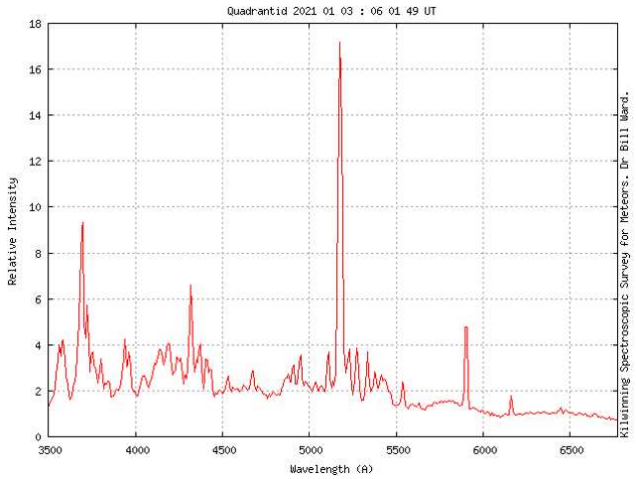

Figure 9 – Quadrantid 2, corrected spectrum graph. Here we have the same prominent lines as in Figure 6 but the Si^{+} at 4131 A is missing.

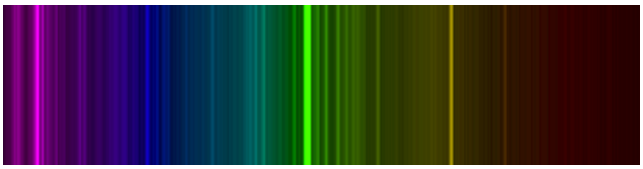

Figure 10 – Quadrantid 2 synthetic colourised spectrum.

2.3 A sporadic meteor

During the Lyrids a very bright spectrum of a non-shower meteor with very unusual characteristics was captured. The spectrum is shown in Figure 11.

The orbit for this meteoroid was obtained by members of the NEMETODE group and is shown in Figure 12 (NEMETODE: Network for Meteor Triangulation

Figure 11 – Spectrum of a sporadic meteor, recorded on 2021 April 21, $22^{h}58^{m}$ UT; video composite image. This spectrum has many Fe lines but the main lines are Fe at 4834 A, Mg triplet at 5174 A a prominent group of Fe lines between 5277 and 5456 A and Na at 5893 A.

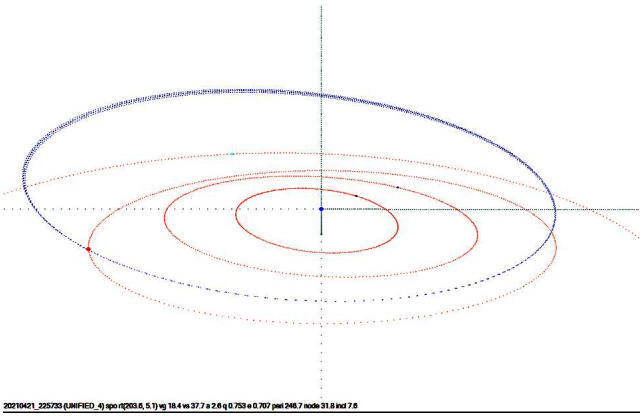

Figure 12 – Sporadic meteoroid orbit plot (courtesy of A. Pratt, NEMETODE).

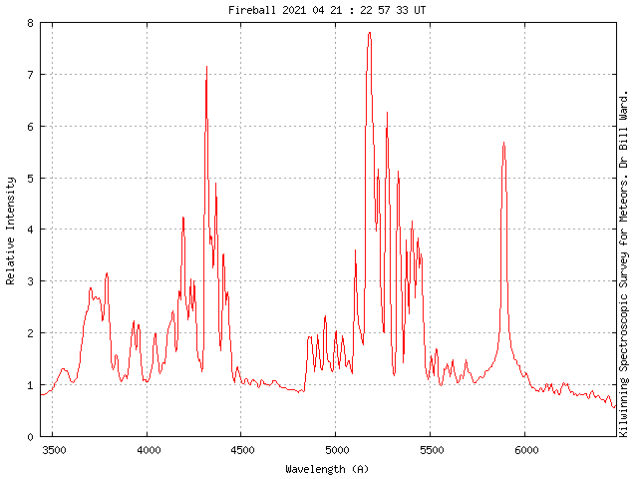

Figure 13 – Sporadic meteor, corrected spectrum graph.

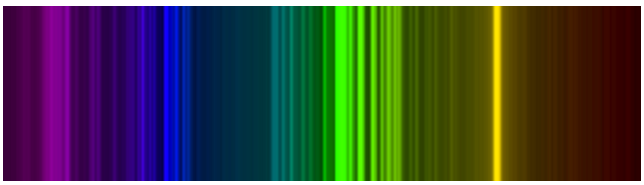

Figure 14 – Sporadic meteor synthetic colourised image.

and Orbit Determination, `http://www.nemetode.org/`) It had a low geocentric velocity of $V_g = 18.4$ km/s. Therefore there Thus, there was less emission from the atmosphere than is normally seen in the spectra of higher velocity meteors. This allowed features which may be unique to this meteor or perhaps are in the spectra of other meteors but masked by the atmospheric emissions lines, to be seen. Of particular interest is the region immediately longward of the sodium doublet at 589 nm. This spectrum has features which are similar to work described by Berezhnoy et al. (2018) and Popov et al. (2021) on the emissions from CaO and FeO in the orange part of the spectrum. The spectrum graph is shown in Figure 13 and the colourised synthetic spectrum is shown in Figure 14.

The spectrum captured here shows good agreement with their modelling and gives a tantalizing glimpse in features that are only visible in rare circumstances. Although the resolution is not quite sufficient for proper resolution some features can be seen in Figure 15.

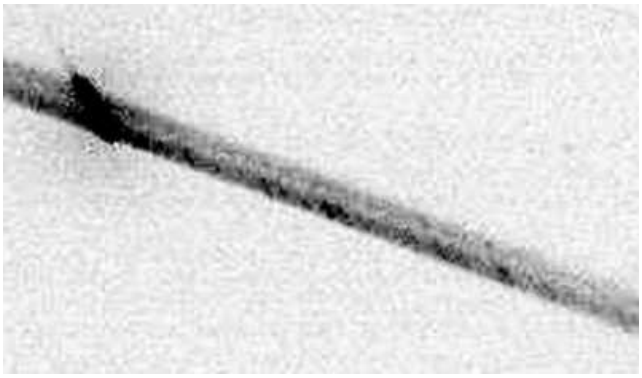

Figure 15 – Sporadic meteor spectrum orange band enlargement.

3 Conclusions

It can be seen that the ASI ZWO174MM is capable of excellent results comparable with the best photographic spectra of past decades (Rendtel, 1993). The routine observations continue with the straightforward goal of capturing as many high resolution and interesting spectra as possible.

Since this presentation was prepared further examples of a variety of meteor compositions have been captured with comparable performance and will be published in due course.

Acknowledgements

The author would like to thank and acknowledge the continued help of, and collaboration with Alex Pratt and the other observers of the NEMETODE group. Alex Pratt coordinated the observations that were used to confirm the identity of the Ursid and Quadrantid meteors as well as the sporadic nature of the final example presented.

References

Berezhnoy A. A., Borovička J., Santos J., Rivas-Silva J. F., Sandoval L., Stolyarov A. V., and Palma A. (2018). "The CaO orange system in meteor spectra". *Planetary and Space Science*, **151**, 27–32.

Popov A. M., Berezhnoy A. A., Borovička J., Labutin T. A., Zaytsev S. M., and Stolyarov A. V. (2021). "Tackling the FeO orange band puzzle in meteor and airglow spectra through combined astronomical and laboratory studies". *MNRAS*, **500**, 4296–4306.

Rendtel J. (1993). *Handbook for photographic meteor observations*. International Meteor Organization, 101–103 pages. IMO Monograph No. 3.

Handling Editor: Jürgen Rendtel

Subspace Based Meteor Detection Using SLIDE

Pete Gural[1]

A feasibility study was performed using an alternative meteor detection algorithm called subspace-based line detection (SLIDE). The method is discussed in the context of existing state-of-the-art, low-light meteor detection algorithms, with the focus on SLIDE's advantages, short-comings, and performance results.

Received 2021 September 29

This work has been presented at the International Meteor Conference 2021 (held online).

1 Introduction

There are many meteor detection algorithms in use today that operate on video meteor imagery. I have been working in the field of real-time meteor detection for over two decades and have developed, evolved, and fine-tuned several innovative approaches in that time. One line detection algorithm in particular has always piqued my interest but seemed a little too complicated to implement when I first came across the paper describing the methodology (Aghajan & Kailath, 1994). The paper described a subspace-based line detection (SLIDE) algorithm that worked in a signal subspace domain that made an analogy between estimating the angle-of-arrival of electro-magnetic plane waves impinging on a straight and uniformly spaced line array of sensors (such as in a radar or communications system), and how that was comparable to performing the detection of lines in a two-dimensional image. Fortunately, a graduate level class in advanced sensor array processing that I was taking at George Mason University in the spring of 2021, had provided the needed background for a more intimate understanding of the algorithm, and the final class project was a good motivating excuse to apply SLIDE on meteor detection.

At the time, there was also another reason to experiment with the algorithm, as it related to my work developing one of the University of Western Ontario's (UWO) image processing pipelines. A program called Detection Application version 2.15 (DetApp for short) has been implemented for Western's very low-light electron multiplying charge coupled device (EM-CCD) cameras. The DetApp processing pipeline development incorporates a number of innovative steps, where the algorithms and performance assessment has now been thoroughly documented in an upcoming paper (Gural et al., 2021). Please refer to this paper for the details which includes an appendix which highlights the various algorithmic processing options for meteor detection. A high-level block diagram of the DetApp processing pipeline's major functional components is provided here and illustrated in Figure 1.

[1]Gural Software and Analysis LLC, Lovettsville, Virginia USA 20180. Email: pgural@gmail.com

IMO bibcode WGN-495-gural-slide
NASA-ADS bibcode 2021JIMO...49..126G

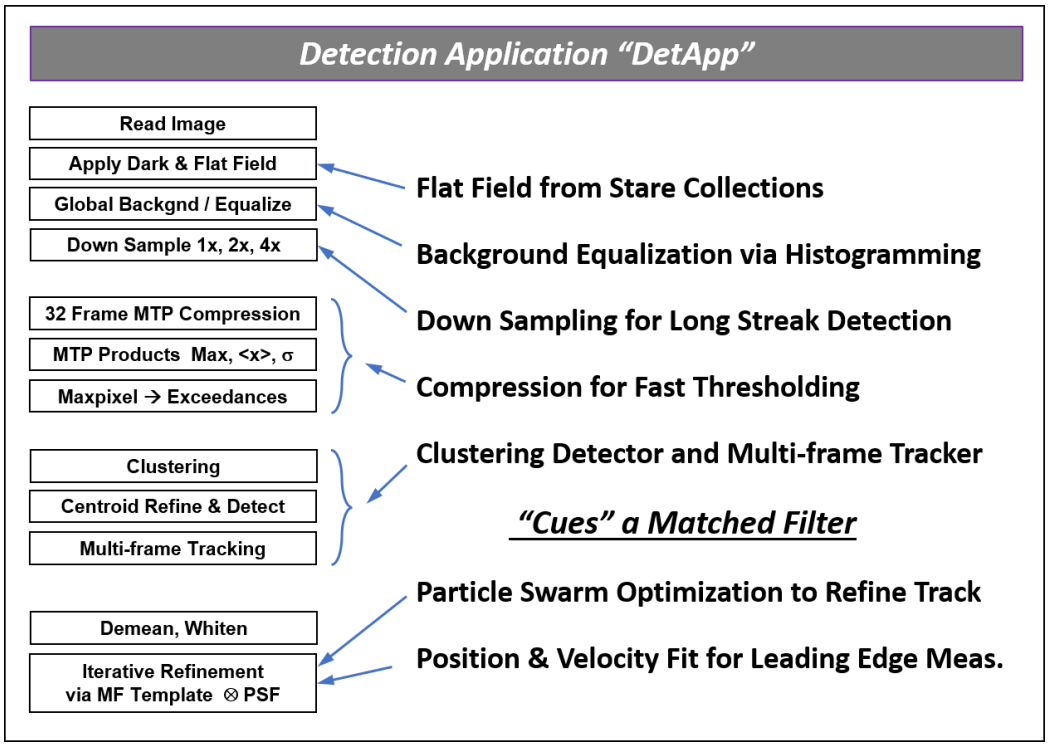

Figure 1 – Major functional blocks and associated innovations in DetApp's image processing pipeline for very faint meteor detection. Refer to Gural et. al 2021 for details.

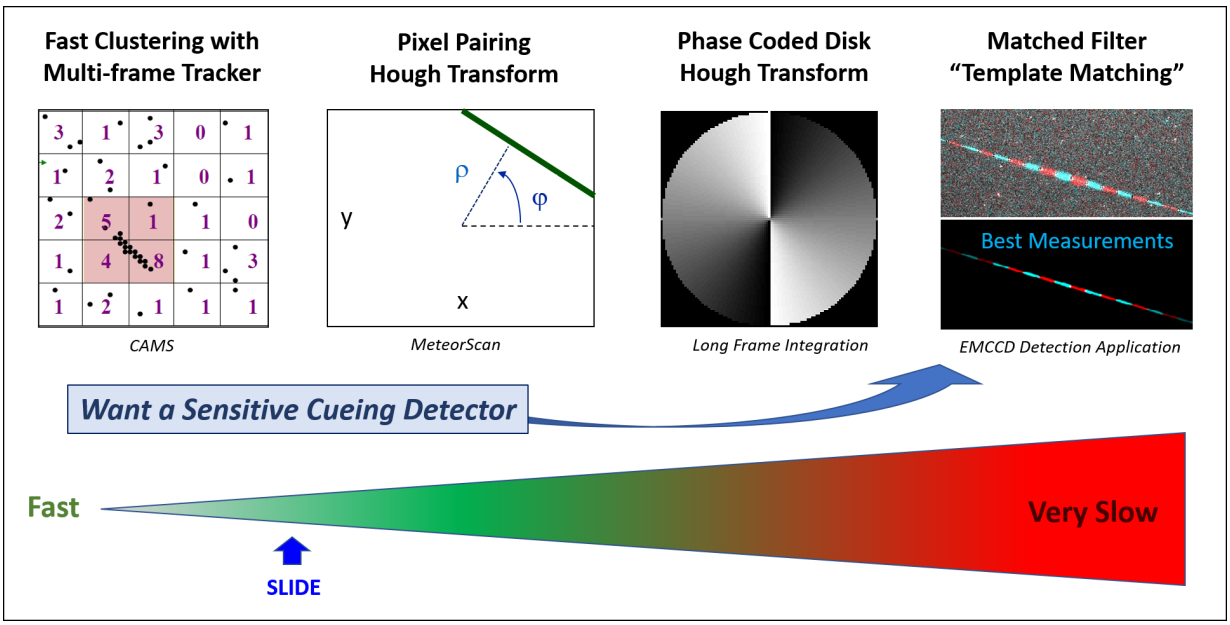

Figure 2 – Relative processing loads of various meteor detection algorithms that could cue a matched filter. SLIDE's estimated performance point fell between fast clustering and pixel-paired Hough transforms.

The critical items of interest in the figure are the very fast clustering and tracking front-end detection module that feeds a computationally intensive matched filter positional refinement step. In the performance evaluation of DetApp, it was found that if the front-end cluster detector was replaced with a full-blown matched filter detector (essentially a template matching algorithm given no a priori information about the meteor), then three times the number of meteors could be detected, gaining close to a magnitude of meteor limiting magnitude. However, a full-blown matched filter took 3 weeks to run on a 64-node cluster to process only 1 hour of imagery. This is because for a matched filter, one must hypothesize templates for ALL realizable directions of meteor motion, speeds, and starting positions. If a fast, but more sensitive front-end detector could be found to replace the existing hierarchical cluster detector, then there could be a significant yield increase in meteors processed into triangulated orbits with the EMCCD system. Realistically, a fraction of the pure matched filter detections were actually so close to the noise background, that generating leading edge pick point measurements would likely be unreliable. But it was felt that a smaller factor of two improvement in detection counts should still produce good quality results.

Other fast algorithms that were considered included MeteorScan's pixel pair Hough transform (Gural, 1999), MetRec's 5×5 kernel matching methodology (Molau, 1999), and the phase coded disk (Clode et al., 2004), with the latter feeding a Hough transform using point-slope contributions. SLIDE's claim to fame is that it is a very computationally efficient algorithm for line detection, allegedly faster than the three just mentioned as depicted in Figure 2, so SLIDE was prototyped in Matlab to be initially tested and evaluated against EMCCD simulated imagery. Note that SLIDE can be applied to either binary thresholded images or gray scale images.

2 The SLIDE Algorithm

As mentioned previously, SLIDE borrows from the field of subspace angle-of-arrival (AOA) methods used in electromagnetic radar and communications systems. The algorithm recasts the mathematical methodology of AOA, as a propagating line that is shifted across columns like a plane wave until it is read out to an imaginary line of sensors at the left edge of the image as visualized in Figure 3. The plane wave analogy to electromagnetic waves is made by introducing a phase term that is column dependent for each pixel. Each

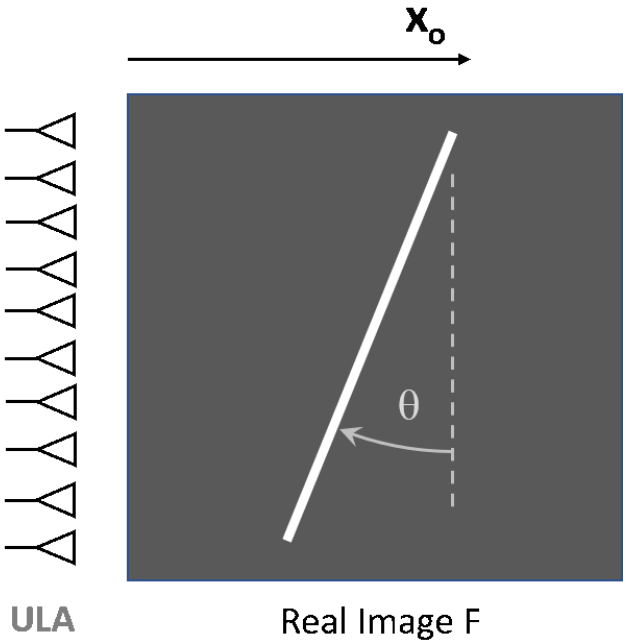

Figure 3 – SLIDE's analogy of using a left side uniform line array (ULA) to gather intensities from a linear streak as pixels are shifted out from right to left like a propagating plane wave.

imaginary sensor for a given row simply represents the sum of the amplitude of the pixels in that row times a phase term given by each pixel's column index $\exp(i * u_o * \text{column})$. This produces an output column vector that is used to build a data matrix. The outer product of the data matrix creates a covariance matrix, that is then eigen-decomposed. The amplitude spread of the eigenvalues define the signal subspace (line information) and the noise subspace (background).

The SLIDE algorithm's next step is to determine the number of lines in the imagery. For that a minimum description length (MDL) algorithm (Wax & Kailath, 1985) was recommended by the SLIDE authors, that utilizes the eigenvalues obtained from the covariance matrix. The resultant output MDL measure of zero, one, or multiple lines in an image is used as the detection metric in this study. Once given the number of lines that may be present in the image, then for each line, the ESPRIT algorithm (Roy & Kailath, 1989) is used to estimate the AOA and column offset position x_o of the line's intersection with the top row. Note that ESPRIT is a super-resolution algorithm so the angle estimation is expected to be very precise.

There are two issues with the SLIDE methodology as originally formulated. First, with the introduction of a phase term, the associated column index scaling factor u_o needs to be selected. The recommendation is to use a value near unity, but this can introduce aliasing in the estimation of angles that are shallower than 45 degrees off the horizontal. One way to mitigate the aliasing is to process both across in rows, and then separately down in columns (or across in rows on the image transpose). This eliminates aliasing for $u_o = 1$ in one of the orthogonal directions, but now a selection needs to be made for the best line estimate if both directions produce an answer. This could be resolved by using the line with the higher eigenvalue.

The second issue is associated with the limited amount of sample support when generating the covariance matrix, as described in the original SLIDE paper. Sample support refers to the amount of independent data realizations that are used to estimate the underlying statistical nature of the problem under investigation. For example, you would prefer to have many samples (lots of sample support) when taking the mean of a set of measurements. The more the better, but one does not always have sufficient numbers of samples to make a robust estimate of the statistics you are trying to model, which was the case in the original SLIDE paper. Fortunately, a follow-on paper was published about a year later (Halder et al., 1995) that added four to five times additional sample support without distorting the signal subspace of the covariance matrix. This worked quite successfully on the test cases performed during this algorithmic study.

3 SLIDE Performance on Simulated Imagery

To assess the performance of SLIDE before committing to an implementation in the DetApp processing pipeline, a prototype Matlab meteor simulation and SLIDE image processing function set were created. The meteor simulation portion mimicked the UWO's EMCCD data characteristics with 512×512 pixel images, containing 5000 stars with PSF halfwidth of 1.13 pixels, a flat white gaussian noise background, and meteor traces with known positions, directions, and constant amplitude across multiple frames. Meteors could appear anywhere in the image moving from 1 to 35 pixels per frame, lasting from 4 to 30 frames, and possess an SNR between 0 and 16 dB. Note that an SNR of 3 dB is just barely visible above the noise.

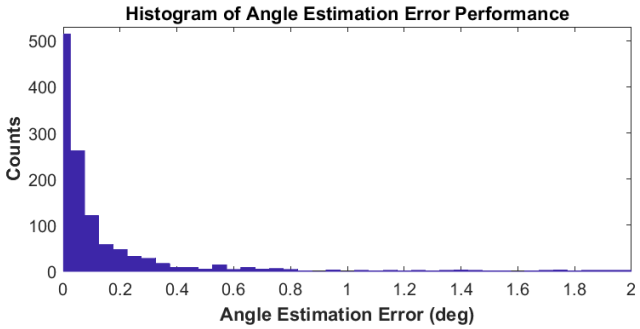

Figure 4 – Histogram of angle estimation errors for SLIDE applied to EMCCD simulated imagery.

The initial SLIDE algorithm implementation and test was performed on a meteor streak that was 25.0 degrees off vertical, which verified the proper functioning of the covariance generation, eigen-decomposition into signal and noise subspace eigenvalues, resultant MDL = 1, with an ESPRIT output for the streak's angle estimation equal to 25.069 degrees. The algorithm was then applied to a large set of simulated meteor imagery with uniform random distributions on position, speed, direction, and amplitude. While the uniform distributions did not represent the true distributions of meteor characteristics that the EMCCD systems encounter, they were purposely selected to cover the full range of realizable meteor characteristics so that performance limits of the algorithm could be assessed.

SLIDE Simulation Results – The Good: Initial results from the simulation study were very promising. As seen in Figure 4, when meteors were detected with SLIDE, the angle estimation of the streaks were often within 0.1 degree of the actual traces and nearly all within 1 degree. This result boded well for using SLIDE as a cueing front-end detector to a matched filter, where the angle estimates and position offsets would help dramatically reduce the number of motion templates that needed to be hypothesized in the matched filter for false alarm reduction and position measurement refinement. Also, it was found that aliasing was only a problem for meteors moving within a very narrow range of 10 degrees off horizontal, which as stated before could be mitigated by transposing the image and processing again.

SLIDE Simulation Results – The Bad: Unfortunately, as shown in Figure 5 that examines the performance limits associated with meteor SNR and length (number of rows the meteor spanned), all the meteors were missed (red x's) at SNR levels below 6 dB and a

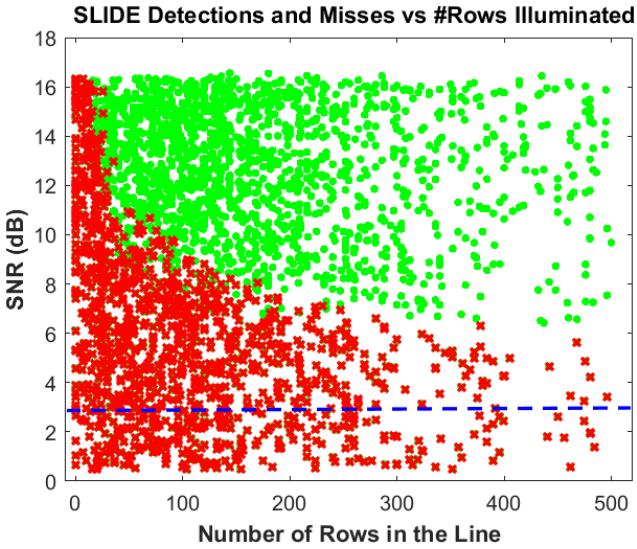

Figure 5 – Detection performance of SLIDE for SNR versus meteor row length where green dots are detections and red x's are missed meteors. The DetApp performance threshold is shown as a blue dashed line at SNR = 3 dB.

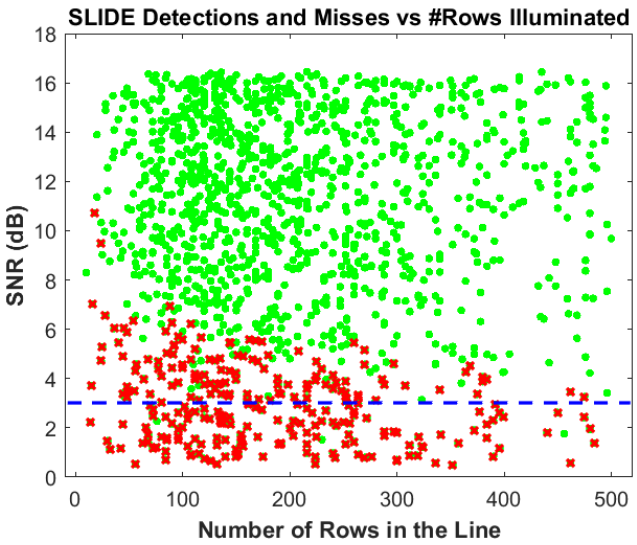

Figure 6 – Detection performance of SLIDE for AOA < 45 degrees and forced MDL = 1. Markers have the same meaning as in Figure 5.

significant number from 6 to 15 dB for shorter length meteors. Those very bright meteors missed above 12 dB, were mostly due to aliasing effects at shallow angles to the horizontal, but that still left a sizeable fraction below 12 dB and less than 200 pixels in row length that were not detected. It should be noted that the DetApp cluster and matched filter processing operates reliably at a 3 dB level across all meteor lengths, which is shown as the blue dashed line in the figure.

SLIDE Simulation Results – The Ugly: To eliminate two effects on the Figure 5 performance results, the simulation was run again. First, the angle of arrival was limited to less than 45 degrees to completely avoid any aliasing contamination issue. Second, the MDL level was forced to be 1 (always a line present) with an angle estimate to be within 3 degrees of true orientation to be declared a good detection. The MDL = 1 test was to see if the MDL detection metric was impacting the result, whose algorithm could have been replaced with another method for estimating the line count in the image set processed. As seen in Figure 6 there is some significant improvement, but still a clear bias of not detecting short meteors that were faint (SNR < 7 dB).

4 Discussion and Conclusions

Clearly the SLIDE algorithm is not performing as well as the existing cluster and tracking algorithm in DetApp. This finding is based on having used a fairly benign simulated image set in the sense that in real video meteor imagery there are typically more artifacts, Poisson type noise rather than Gaussian, and variable intensity light curves of meteors.

The SLIDE algorithm was found to generally miss shorter and fainter meteors. However, the performance is extremely good when a meteor spans all the rows of the image. This performance behavior is conjectured to be due to a breakdown of an assumption that was not explicitly stated in the SLIDE paper. Use of a plane wave analogy for imagery lines within the core algorithm's derivation, must imply an image streak must span the entire focal plane for the algorithm to work optimally. Meteors in general do not span an entire focal plane, even over multiple frames and thus the SLIDE algorithm behaves sub-optimally.

Given that finding, variations of the processing were tried such as working on a subset of the image strictly around the meteor (streak spanned the image chip out), but that did not yield any better results. Thus, there must also be a multi-row aggregation effect, that improves detection performance as more row pixels possessing signal intensities are combined together.

In general, the findings of this study were as follows:

- SLIDE provides excellent angle estimation when meteors are detected
- One may need to find an alternate line count detection metric than the MDL algorithm
- SLIDE generally misses short and faint meteors, but is effective for spatially long meteors

Overall, SLIDE's sensitivity performance was found to be worse than the front-end detector used in the current EMCCD processing pipeline DetApp. Thus, it is not a viable candidate to replace the current fast hierarchical cluster detector, as a more sensitive front-end processing algorithm to cue the matched filter. Other algorithmic suggestions are welcome.

References

Aghajan H. and Kailath T. (1994). "SLIDE: Subspace-based Line Detection". *IEEE Trans on PAMI*, **16:11**, 1057–1073.

Clode S. P., Zelniker E. E., Kootsookos P. J., and Clarkson I. V. L. (2004). "A phase coded disk approach to thick curvilinear line detection". In *12th European Signal Processing Conf. IEEE*. pages 1147–1150.

Gural P. (1999). "MeteorScan documentation and user's guide version 2.2". http://aquarid.physics.uwo.ca/~pbrown/METEORSCAN.pdf .

Gural P., Mills T., Mazur M., and Brown P. (2021). "Development of a Very Faint Meteor Detection System based on an EMCCD Sensor and Matched Filter Processing". *Experimental Astronomy*. (in review).

Halder B., Aghajan H., and Kailath T. (1995). "Propagation Diversity Enhancement to the SLIDE Algorithm". In *Proceedings of the SPIE 2424, Non-Linear Image Processing IV*. pages 320–328.

Molau S. (1999). "The meteor detection software MetRec". In *Meteoroids 1998*, Bratislava. Astron. Inst. Slovak Acad. Sci., pages 131–134.

Roy R. and Kailath T. (1989). "ESPRIT – Estimation of Signal Parameters via Rotational Invariance Techniques". *IEEE Trans on ASSP*, **37:7**, 984–995.

Wax M. and Kailath T. (1985). "Detection of Signals by Information Theoretic Criteria". *IEEE Trans on ASSP*, **33:2**, 387–392.

Handling Editors: Jeremie Vaubaillon and Javor Kac

The Fruits of Failure, Frustration and Fortune – Two years in an amateur meteor observer's life

Peter C. Slansky[1]

In this presentation (to be taken 99 % seriously) the author described his observations of meteors and related phenomena during the last two years with a variety of observation techniques with large-sensor video cameras. At that, failure, which again and again led to frustration, but also fortune played the decisive role.

Received 2021 October 4

This work has been presented at the International Meteor Conference 2021 (held online).

1 Introduction

The year 2020 had started quite successful with my most fruitful Quadrantids observation campaign ever. Bernd Gährken and I had gone to Southern Tyrol. In the night from January 3rd to 4th my Sony a7S, equipped with my new meteor universal weapon, a Sony 1.4/24 mm GM lens, recorded 308 meteors in 4:45 hours, 209 of them Quadrantids – a personal record. One night later we set up our telescopes for moon impacts. We could record two hours of video of the dark side of the Moon (phase 0.644). The inspection of the videos turned out to be quite a task. Moon impacts are very difficult to detect by software because they are so short, with a duration of only a few frames. So, I generated sum images with the maximum brightness function of each two minutes of the video. And small bright spots showed up in the sum images! We were already cheering and opening a bottle of champagne – but inspection of the original video files revealed that, instead of lunar impacts, all the camera had captured were so called cosmics that show up only in one frame. And there were plenty of cosmics.

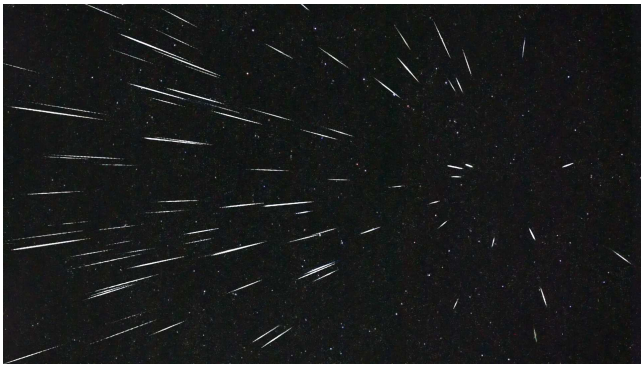

Figure 1 – Composite image of 84 Quadrantids 2020 recorded from Southern Tyrol with a Sony a7S with a Sony GM 1.4/24 mm lens.

Driven by frustration, I set up a concept of a cubic arrangement of my three Sony a7S as an in situ detector for cosmic particles. However, project 3APES (Triple Atomic Particles Examination System) turned out to be quark. Tests of my three cameras revealed, that cameras 2 and 3 detected 6 and 7 particles per minute, respectively, but in the very same time interval camera 1 detected 14! This camera had been modified by removing the UV/IR cut filter being replaced by a clear glass. My suspicion was that many of the so called cosmics of camera 1 had not travelled a long way through

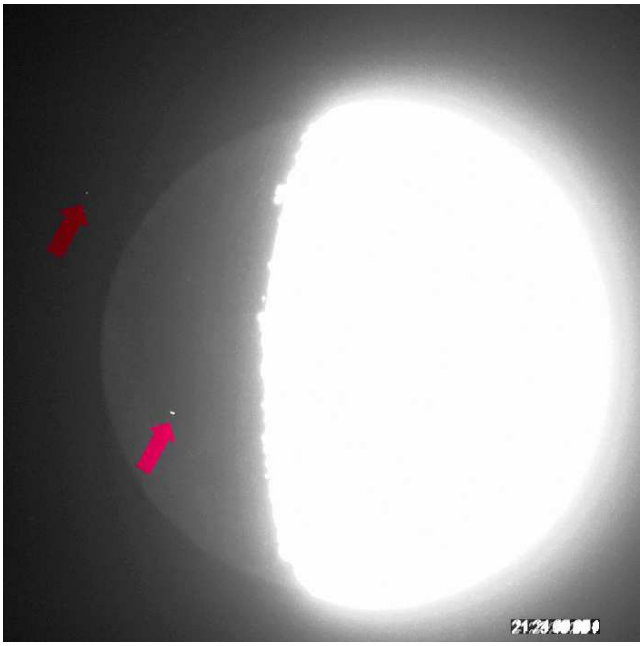

Figure 2 – Quadrantids 2020: What looked as possible moon impacts in the sum image of two minutes of video turned out to be so called cosmics.

Figure 3 – Setup for project 3APES (Triple Atomic Particles Examination System): Three Sony a7S in a cubic array as an in situ particles detector. The failure of this project is described in the main text.

[1]Department II Technology, University for Television and Film Munich. Email: slansky@mnet-online.de

IMO bibcode WGN-495-slansky-fruits
NASA-ADS bibcode 2021JIMO...49..131S

Figure 4 – My one and only 2021 Eta Aquarid. I recorded it from my roof terrace in Munich two nights after the maximum with a Sony a7S with a Sony GM 1.4/24 mm lens.

the universe to the sensor but just a short way from the coating of this glass. Frustration!

Lyrids came. Bernd Gährken, Matthias Knülle and I set up a three-station observation for April 21st/22nd with me in Munich in the West, Matthias in Loitersdorf in the middle and Bernd at Sudelfeld in the East. We all had quite good viewing conditions. From the light polluted Munich city centre my Sony a7S, now equipped with a 2.8/15 mm fish eye lens, recorded 59 meteors in 3:38 hours, 41 of them Lyrids – a personal record, again. The brightest Lyrid recorded by all our cameras fell $00^{\mathrm{h}}26^{\mathrm{m}}$ UT. Jürgen Michelberger made a trajectory calculation.[a] Fortune!

The most spectacular observation in my first Corona year 2020 came completely out of the blue. On the evening of July 5th I stepped out to my roof terrace to take a last look around. At that evening at $20^{\mathrm{h}}30^{\mathrm{m}}$ UT I saw the very first noctilucent clouds of my life – and what a display it was! The NLCs reached from horizon to horizon from the West to the East. Their brightness clearly surpassed the Munich city lighting, even that of the cathedral, which is illuminated as bright as day. It took me a while to realize that these were NLCs, so far in the South. Then I got my cameras ready... I wrote an article for WGN journal (Slansky, 2020) and made the NLCs the subject of my presentation on 2020 online IMC.

One year later I was prepared better. For more than a fortnight, I kept a lookout every evening at $22^{\mathrm{h}}00^{\mathrm{m}}$, and at $03^{\mathrm{h}}00^{\mathrm{m}}$ the alarm clock rang. Cameras were ready. But it turned out that the NLCs on July 2nd/3rd were the only ones in Munich in 2021, showing only a minor display. I made photo series in the visual light, near infrared and UV-A. Results were not really significant. A stereoscopic composite image with a photo series made by Bernd failed.

My planned observations of the Perseids, Leonids and Orionids became victim of bad weather. But Geminids 2020 turned out to be blast. Bernd and I went to Osterhofen/Bavaria. During 2:25 hours of video I could record 243 meteors, among them 175 Geminids[b]. We saw no fireballs, but: Fortune again.

2020 Northern Taurids and Alpha Monocerotids, as well as 2021 Quadrantids and Eta Aquarids all failed due to bad weather. So, frustration, again... But wait a minute: Two nights after the Eta Aquarids maximum I was able to record 1:45 hours video – and happily enough: There was one Eta Aquarid[c]. My only one till today, but, well, a little bit of fortune.

That was the point, when I was struck by the insight that the scientific term for fortune is coincidence! And – imagine my utter bewilderment! – I watched my one right hand write down:

$$E = mc^2$$

In this formula E is the efficiency of a meteor observation, m the methodology and c the coincidence. I think it is valid only for amateur observations. For professionals it might be E equals m^2 times c, but I am not sure. I have to go through the math again, it is so complex...

In the light of this groundbreaking discovery, I went in search of an object that was moving with meteor speed but was totally predictable. So, I found that the International Space Station ISS was worthy of my cinematography. You can find my video of an overfly of the ISS over Munich here: `https://vimeo.com/476651368` (looking forward for your clicks, comments, likes and links). For this video I used a professional ARRI Alexa film camera from my University at the 0.8 m altazimuth Cassegrain telescope of the Munich public observatory (Volkssternwarte München). With a focal length of 8 000 mm and a sensor size of 24×13.5 mm, the field of view was only $10.3' \times 5.8'$. It was totally clear that the telescope had to be controlled absolutely precisely.

[a] `https://www.imo.net/members/imo_photo/view?photo_id=1505`

[b] `https://www.imo.net/members/imo_photo/view?photo_id=1793`

[c] `https://www.imo.net/members/imo_photo/view?photo_id=1876`

Figure 5 – Still images from the ISS video shot on September 30th 2020.

Figure 6 – For the video of a fly over of the ISS over Munich I used a professional film camera ARRI Alexa M on the 800/8000 mm altazimuth Cassegrain telescope of the Munich public observatory (Volkssternwarte München). The first four trials failed because ISS flew out of the field of view only $10.3' \times 5.8'$.

Figure 7 – Setup for project 3CAMPI – CF (3-Camera Measurement of the Population Index with Concentric Fields for the Perseids 2021. Camera 1 was equipped with a Sony GM 1.4/24 mm, camera 2 with a Zeiss Planar 1.4/85 mm and camera 3 with a Canon 2.8/400 mm tele lens.

This was done by the programmer of the steering Klaus Nagel, personally. Needless to say, that, before we succeeded on September 30th 2020 on the fifth try, we had four frustration failures at first. But a ratio of 1:5 should be considered to be good fortune.

Still work in progress is the evaluation and interpretation of my video observations of this year's Perseids. On the IMC 2018 I had presented my project 3CAMPI (3-CAmera Measurement of the Population Index): three Sony a7S with identical 50 mm lenses pointing to the identical field of view but with different ND filters for different limiting magnitudes at the same signal-to-noise ratio (Slansky, 2019). This year I realised follow-up project 3CAMPI – CF: again, three Sony a7S, but this time equipped with three lenses of different focal lenses, all pointing to the radiant with Concentric Fields. The goal was, again, to see how far the population index remains constant to faint shower meteors. Camera 1 was equipped with a 1.4/24 mm wide angle, camera 2 with a 1.4/85 mm tele and camera 3 with a 2.8/400 mm tele (providing an entry pupil of 140 mm diameter!). Due to a frustrating series of technical problems as well as passing clouds, I was only able to capture 2:15 hours of video in two nights in South Tyrol. Camera 1 reached a stellar limiting magnitude of 7.2 mag, camera 2 reached 9.1 mag and camera 3 more than 11 mag. But camera 1 recorded 267 meteors, among them 147 Perseids, camera 2 recorded 93 meteors and 43 Perseids and camera 3 recorded 21 meteors among them 4 Perseids (with the assignment quite difficult). This result came as something of a surprise to me; it needs to be investigated in more detail. So, I ended my IMC presentation with three question marks.

As a conclusion of what has been described for the last two years, I am now trying to proceed from $E = mc^2$ to $E = m^2c$. But that might fail in a frustrating way – or require a lot of fortune...

References

Slansky P. C. (2019). "SCAMPI – Single CAmera Measurement of the Population Index". In Rudawska R., Rendtel J., Powell C., Lunsford R., Verbeeck C., and Knöfel A., editors, *Proceedings of the International Meteor Conference, Pezinok-Modra, Slovakia, 2018, August 30 – September 2*. International Meteor Organization, pages 17–21.

Slansky P. C. (2020). "Noctilucent clouds over Munich in July 2020". *WGN, Journal of the IMO*, **48:5**, 150–157.

Handling Editor: Javor Kac

Mobile Observation of Meteors (MoMET): a device dedicated to meteor shower outburst

P. Da Fonseca[1], *J. Vaubaillon*[1], *F. Bouley*[2], *G. Fasola*[2], *K. Baillié*[1], *J. Desmars*[1], *J. Ph. Amans*[2]

The MoMET project aims to observe meteor shower outbursts by setting up two mobile stations. In order to make the most of such endeavour, two suitcases were developed, each containing 2 wide FOV cameras for ZHR determination, and 3 narrow FOV cameras for orbit measurement and spectroscopy. The RMS software for acquisition and detection was installed on Odroid XU4Q mini-computers running Ubuntu. A user interface allows to control each camera and a GPS to set the time and location.

Received 2021 October 18

This work has been presented at the International Meteor Conference 2021 (held online).

1 The MoMET project

1.1 Introduction

The observation of recurrent meteor outbursts provide insights about their origin, age, parent body identification and behaviour (e.g. outgassing), composition and about their evolution in the Solar System (dynamics). Although wide spread meteor camera network survey a large surface of atmosphere (Devillepoix et al., 2020; Vida et al., 2021), the orbital geometry might not always allow the record of a specific outburst. One recent example is the new shower caused by comet 15P/Finlay (Ye et al., 2015; Vaubaillon et al., 2020), observable from South America where there is a limited number of meteor cameras (Tóth & Kaniansky, 2016). It is therefore very useful to deploy a mobile camera network on the ground to fully cover an exceptional event (e.g. Atreya & Christou, 2009; Vaubaillon et al., 2015). In addition, due to bad weather conditions, it is sometimes useful to change the observation site when it is not possible to operate from above the clouds (Rambaux et al., 2021). The "Mobile Observation of Meteor" (MoMET) project aims to easily deploy such a local and mobile network of cameras, in a timely and scientifically efficient way.

1.2 Scientific goals and means to achieve them

Optical observations of meteors allow to constrain the following properties :

G.1 parent activity, meteoroid lifetime expectancy

G.2 meteoroid formation

G.3 meteoroid composition

G.4 meteoroid tensile strength

G.5 comet or asteroid link

G.6 origin of meteoroid stream

G.7 age of meteoroid stream

Scientific goals G.1 and G.2 are accessed with wide field of view (WFOV) cameras, by measuring the ZHR (Koschack & Rendtel, 1990). G.3 is accessible thanks to low resolution spectroscopy, implying a narrow field of view (NFOV) camera equipped with a grating. G.4, G.5, G.6 and G.7 necessitate a double-station setup, preferably with NFOV cameras for better accuracy.

In order to fulfill all these goals, the MoMET project involves two suitcases each containing 2 WFOV cameras, and 3 NFOV cameras, one of which is equipped with a 600 l/mm grating. The relative pointing directions of the suitcases (and – inside – of the cameras) are optimized to observe the widest atmosphere area given the scientific constraints.

2 Development

2.1 Hardware

A MoMET suitcase is equipped with IMX174-based cameras (either Basler acA1920-155um or DMK 33UX174), with 6- or 12-mm lenses (for WFOV and NFOV respectively). The control mini-computers are either Odroid XU4Q or RaspBerry-pi 4. An ethernet switch connects all the cameras to the same network. The user takes control of the cameras through the mentioned switch. A mechanical structure was designed and built, that allows the folding and unfolding of the cameras. The electrical power is ensured either from power outlet or from a car battery. In the latter case, we estimate the observation can run for about 8 hrs with a full battery. A GPS antenna provides time and location. Figure 1 shows one MoMet suitcase.

2.2 Software

The acquisition and meteor detection is ensured by the RMS software (Vida et al., 2016; Vida et al., 2021). In order to adapt RMS to Odroid mini-computers, a temporary SWAP memory was added. We use the Gstreamer[a] and Aravis[b] libraries to handle genicam-type cameras. One of the 5 mini-PC is equipped with a

[1]IMCCE, Observatoire de Paris, PSL Research University, CNRS, Sorbonne Universités, UPMC Univ. Paris 06, Univ. Lille., France. Email: pedro.da-fonseca@epitech.eu

[2]Pole instrumental du GEPI, Observatoire de Meudon, France.

IMO bibcode WGN-495-dafonseca-momet
NASA-ADS bibcode 2021JIMO...49..134D

[a]https://gstreamer.freedesktop.org/documentation/video

[b]https://github.com/AravisProject/aravis

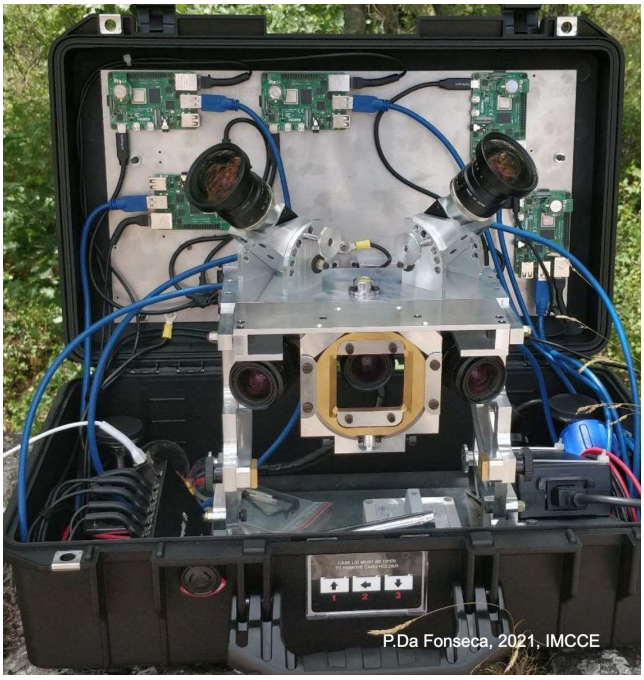

Figure 1 – Deployed MoMET suitcase (P. Da Fonseca, IMCCE).

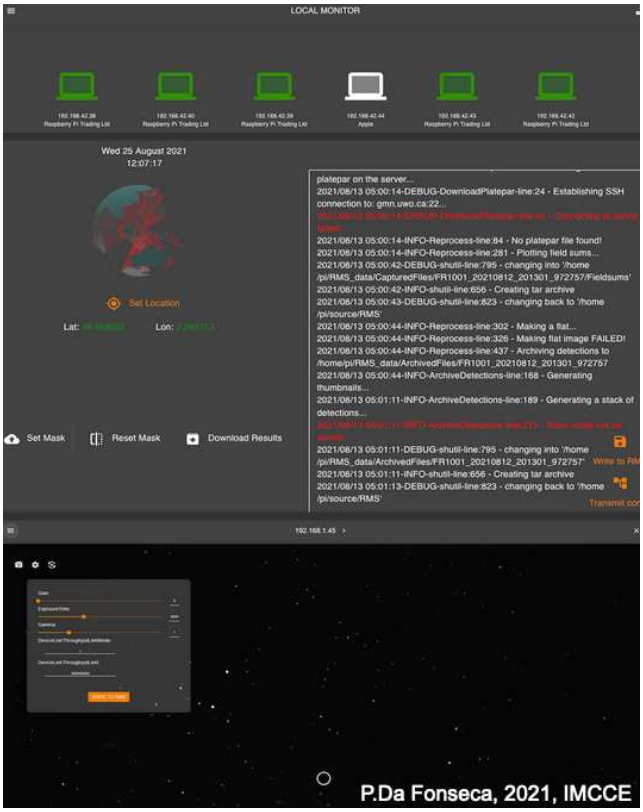

Figure 2 – Screenshot of the The MoMET GUI in operation (P. Da Fonseca, IMCCE).

DHCP server, allowing the user to take control of each camera, set the RMS parameters, get a live view of the camera (for pointing, focusing and demasking purposes) and set the time with a ms precision (XBU-353). Figure 2 shows the MoMET GUI.

3 Conclusion

The "Mobile Observation of Meteors" was tested during several test campaigns. At the time this paper is written, the 2 MoMET cases are in Chile for the record of the new meteor shower caused by comet 15P/Finlay, as predicted by Vaubaillon et al. (2020). Tutorials are available to learn how to operate the MoMET suitcase[c]. The software codes are freely available (upon request) on gitlab.

The astrometry will be performed using SkyFit2, from the RMS distribution. Meteoroid orbit calculations will be performed using either Vida et al. (2018) or Egal et al. (2017) methods.

Acknowledgements

The MoMET project is led and supported by IMCCE/Observatoire de Paris / PSL. This work was also supported by the Programme National de Planétologie (PNP) of CNRS-INSU.

References

Atreya P. and Christou A. A. (2009). "The 2007 Aurigid meteor outburst". *MNRAS*, **393:4**, 1493–1497.

Devillepoix H. A. R., Cupák M., Bland P. A., Sansom E. K., Towner M. C., Howie R. M., Hartig B. A. D., Jansen-Sturgeon T., Shober P. M., Anderson S. L., Benedix G. K., Busan D., Sayers R., Jenniskens P., Albers J., Herd C. D. K., Hill P. J. A., Brown P. G., Krzeminski Z., Osinski G. R., Aoudjehane H. C., Benkhaldoun Z., Jabiri A., Guennoun M., Barka A., Darhmaoui H., Daly L., Collins G. S., McMullan S., Suttle M. D., Ireland T., Bonning G., Baeza L., Alrefay T. Y., Horner J., Swindle T. D., Hergenrother C. W., Fries M. D., Tomkins A., Langendam A., Rushmer T., O'Neill C., Janches D., Hormaechea J. L., Shaw C., Young J. S., Alexander M., Mardon A. D., and Tate J. R. (2020). "A Global Fireball Observatory". *PLANSS*, **191**, 105036.

Egal A., Gural P. S., Vaubaillon J., Colas F., and Thuillot W. (2017). "The challenge associated with the robust computation of meteor velocities from video and photographic records". *Icarus*, **294**, 43–57.

Koschack R. and Rendtel J. (1990). "Determination of spatial number density and mass index from visual meteor observations (I).". *WGN, Journal of the IMO*, **18:2**, 44–58.

Rambaux N., Vaubaillon J., Derelle S., Jacquart M., Millet M., Lacassagne L., Petreto A., Simoneau P., Baillié K., Desmars J., Galako D., and Chotin R. (2021). "Meteorix camera tests for space-based meteor observations". *WGN, Journal of the IMO*, **49:5**, 142–144.

[c] `https://www.youtube.com/playlist?list=PL5_hsURFgP_AbYmAVuokJqeTypMU1ltsd`

Tóth J. and Kaniansky S. (2016). "Expedition Atacama - project AMOS in Chile". In Roggemans A. and Roggemans P., editors, *International Meteor Conference Egmond, the Netherlands, 2-5 June 2016*. page 295.

Vaubaillon J., Egal A., Desmars J., and Baillié K. (2020). "Meteor shower output caused by comet 15P/Finlay". *WGN, Journal of the IMO*, **48:2**, 29–35.

Vaubaillon J., Koten P., Margonis A., Toth J., Rudawska R., Gritsevich M., Zender J., McAuliffe J., Pautet P.-D., Jenniskens P., Koschny D., Colas F., Bouley S., Maquet L., Leroy A., Lecacheux J., Borovicka J., Watanabe J., and Oberst J. (2015). "The 2011 Draconids: The First European Airborne Meteor Observation Campaign". *Earth Moon and Planets*, **114:3-4**, 137–157.

Vida D., Brown P. G., and Campbell-Brown M. (2018). "Modelling the measurement accuracy of pre-atmosphere velocities of meteoroids". *MNRAS*, **479**, 4307–4319.

Vida D., Šegon D., Gural P. S., Brown P. G., McIntyre M. J. M., Dijkema T. J., Pavletić L., Kukić P., Mazur M. J., Eschman P., Roggemans P., Merlak A., and Zubović D. (2021). "The Global Meteor Network - Methodology and first results". *MNRAS*, **506:4**, 5046–5074.

Vida D., Zubović D., Šegon D., Gural P., and Cupec R. (2016). "Open-source meteor detection software for low-cost single-board computers". In Roggemans A. and Roggemans P., editors, *International Meteor Conference Egmond, the Netherlands, 2-5 June 2016*. page 307.

Ye Q.-Z., Brown P. G., Bell C., Gao X., Mašek M., and Hui M.-T. (2015). "Bangs and Meteors from the Quiet Comet 15P/Finlay". *APJ*, **814:1**, 79.

Handling Editor: Javor Kac
This paper has been typeset from a LaTeX file prepared by the authors.

Simultaneous broadband radio and optical emission of meteor trains imaged by LOFAR / AARTFAAC and CAMS

Tammo Jan Dijkema[1], *Cees Bassa*[1], *Mark Kuiack*[2], *Peter Jenniskens*[3], *Carl Johannink*[3], *Felix Bettonvil*[4], *Ralph Wijers*[2], *Richard Fallows*[1]

We report on simultaneous 30 – 60 MHz LOFAR / AARTFAAC12 radio observations and CAMS low-light video observations of +4 to −10 magnitude meteors at the peak of the Perseid meteor shower on August 12/13, 2020. 204 meteor trains were imaged in both the radio and optical domain. Aside from scattered artificial radio sources, we identify broadband radio emission from many persistent trains, one of which lingered for up to 6 minutes. Unexpectedly, fewer broadband radio meteor trains were recorded when the experiment was repeated during the 2020 Geminids and 2021 Quadrantids. Intrinsic broadband radio emission was reported earlier by the Long Wavelength Array, but for much brighter meteors and observed with lower spatial resolution. The new results offer insight into the unknown radio emission mechanism.

Received 2021 November 3

This work has been presented at the International Meteor Conference 2021 (held online).

1 Introduction

Meteors are well-known to reflect artificial radio emission in forward and backward scattering. Combined optical and radio meteor scatter observation of meteors go back to (Prentice et al., 1947), showing that meteor trains are overdense for most visible meteors. Forward meteor scatter, where transmitter and receiver are not at the same location, can be used to study meteors as is done in, e.g., the Belgian RAdio Meteor Stations (BRAMS) network (Lamy et al., 2011).

Less well established is the detection of intrinsic natural radio emission from the meteor or meteor train itself. Early efforts to detect intrinsic emission relied on temporal coincidences (e.g., Price & Blum (2000)). The first more substantive reports based on radio imaging came from all-sky imaging at low radio frequencies (∼40 MHz) with the Long Wavelength Array, detecting intrinsic non-thermal radio emission from fireballs (Obenberger et al., 2014; Obenberger et al., 2016a; Obenberger et al., 2016b). The emission persisted well after the meteor itself had faded. The emission mechanism of these meteor radio afterglows is not fully understood, and so far has not been independently confirmed with other instruments. A survey with the Murchison Widefield Array (Zhang et al., 2018) did not show this intrinsic emission at higher 72–103 MHz frequencies.

Several mechanisms for broadband radio emission from meteors have been suggested in the literature, namely reflected broadband terrestrial radio emission, intrinsic emission from chemically produced suprathermal electrons (Obenberger et al., 2020), Langmuir waves (Obenberger et al., 2015), free-free emission (Filonenko, 2018) and transition radiation (Obenberger et al., 2020). Also, bright celestial radio emission shines on the meteor trains and that radiation may be scattered, as suggested in Obenberger et al. (2015).

Here we report on low-frequency all-sky observations with the LOFAR ("Low Frequency Array") radio telescope (van Haarlem et al., 2013) during the 2020 Perseid meteor shower (Jenniskens, 2006). The radio data are complemented with simultaneous, both temporally and spatially, optical video observations from the CAMS BeNeLux network (Jenniskens et al., 2011) in an effort to study the altitude dependence of the proposed intrinsic radio emission.

2 Observations

The LOFAR radio telescope consists of thousands of dipole antennas grouped into stations spread over Europe, with a dense core of stations located in the North of the Netherlands. Each LOFAR station has low-band antennas (LBAs) which can observe from 10 to 90 MHz and high-band antennas (HBAs) operating from 110 to 250 MHz. During regular LOFAR LBA observations radio signals are combined (beamformed) hierarchically, by first combining radio signals from dipole antennas in a station, and then combining or correlating the combined radio signals from stations to increase sensitivity at the expense of field-of-view.

The AARTFAAC piggyback instrument (Prasad et al., 2016; Kuiack et al., 2019; Kuiack et al., 2021) provides a special observing mode whereby LOFAR can create all-sky images of the radio sky. It does so by correlating the radio signals from all 576 LBA dipoles from the inner 12 LOFAR stations located in the dense core (with a 1.2 km diameter) surrounding the "super terp" in Drenthe, the Netherlands, see Figure 1.

LOFAR/AARTFAAC observations were obtained during the Perseid meteor shower (2020 August 12-13) for 64 frequency channels of 48.8 kHz bandwidth (grouped into 16 subbands of 4 channels each), spread over radio frequencies between 30 to 60 MHz. These observations were used to create all-sky images with 3′ spatial resolution and 2 s time resolution.

All-sky radio images were created for each of the individual AARTFAAC subbands (a set of 4 channels). This analysis used a newer version of the pipeline de-

[1]ASTRON, Netherlands Institute for Radio Astronomy
[2]Anton Pannekoek Institute, University of Amsterdam
[3]SETI Institute
[4]Leiden University / NOVA

IMO bibcode WGN-495-dijkema-radio-optical
NASA-ADS bibcode 2021JIMO...49..137D

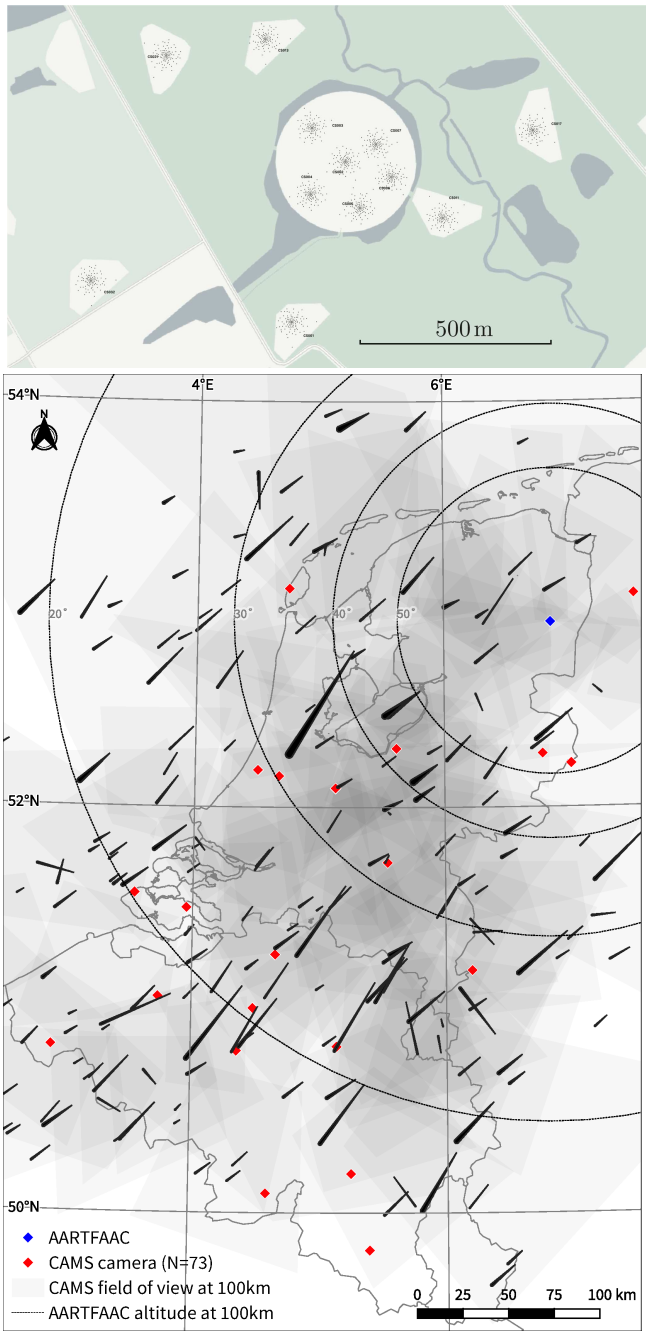

Figure 1 – Top: map of the LOFAR core with the location of all 512 dipole antennas used for AARTFAAC. Bottom: map with CAMS camera locations (red), the location of the LOFAR core (blue) and co-observed meteors.

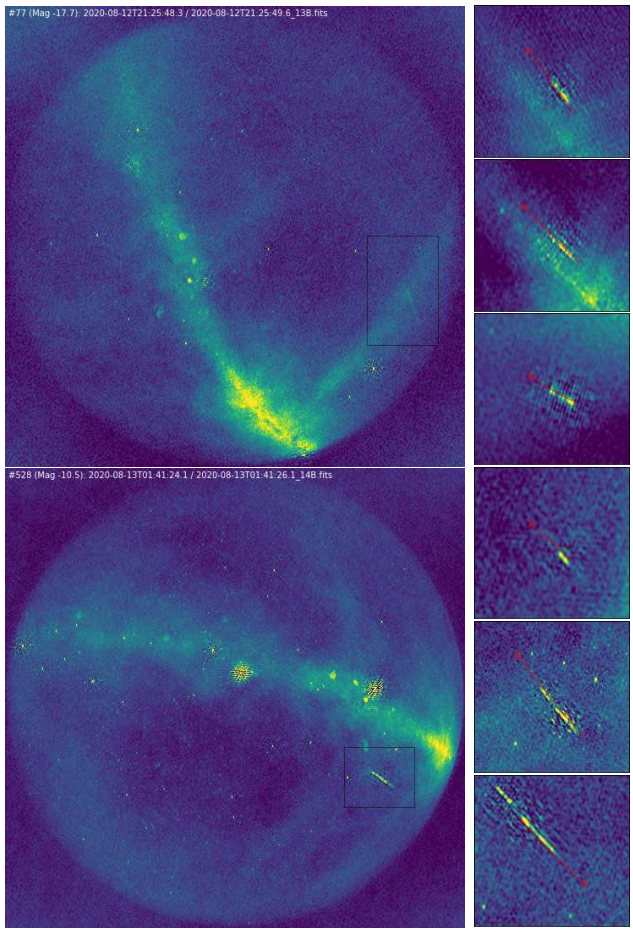

Figure 2 – AARTFAAC image (integrated over all observing bands) of the meteors at 2020-08-12 21:25:48 UTC (top left) and 2020-08-13 01:41:24 UTC (bottom left). The large-scale diffuse emission is the Galactic plane, the bottom left image shows some residuals of the subtracted sources Cassiopeia A and Cygnus A. The right column shows zoomed in meteors, from top to bottom corresponding to numbers 144, 235, 249, 317, 333, and 704 in the CAMS data set. In red, the trajectory as computed from the CAMS optical observations is overlaid.

scribed in (Shulevski et al., 2021). As part of the pipeline, the brightest radio sources Cassiopeia A and Cygnus A were subtracted, to minimize imaging artefacts across the all-sky images. Typically, in subbands containing strong narrow-band terrestrial radio emission reflected by meteor ionization trails, such as emission from the BRAMS meteor forward scatter network transmitter in Belgium near 50 MHz (Lamy et al., 2016), the imaging failed, and images from these subbands were rejected. Images from the remaining subbands were averaged in radio frequency across subbands. This resulted in 10713 all-sky radio images at a 2 s cadence, corresponding to 5 h of data. Example all-sky images obtained with AARTFAAC are shown in Figure 2. A full time-lapse of these images is available as (Dijkema et al., 2021b).

The CAMS BeNeLux low-light video network is part of the global ("Cameras for Allsky Meteor Surveillance") network and uses close to 100 low-light video cameras spread over the BeNeLux to triangulate optical meteors +4 and brighter using methods described in Jenniskens et al. (2011). Weather was clear during the night of 2020 August 12-13 and the trajectory and orbits of 720 meteors were measured (Roggemans, 2020).

Figure 2 shows a subset of these meteor trajectories overlaid on the all-sky radio images from the perspective of the "super terp". All all-sky radio images within a few seconds of CAMS detections were inspected manually for radio emission coincident with the reconstructed meteor trajectory. This resulted in 204 meteors where radio emission was coincident with a CAMS detection. Of these meteors, 59 had a discernible trail in the radio images, the others showed up as point-like in the radio images. There were also dozens of radio meteors without a counterpart in the CAMS data, mostly due

to missing sky coverage of CAMS in Germany at the time, see Figure 1.

For each radio meteor coincident with a CAMS detection we have determined the begin and end point of the radio trail in the all-sky radio images and the duration for which the meteor was visible in the radio images.

3 Results

The coincidence of optical and radio trails demonstrates that meteors are a source of radio emission, be it scattering or intrinsic emission. That emission can last up to minutes; the longest radio train we have observed lasted 6.5 min, coincident with a CAMS meteor detection with optical magnitude of −9. In general, we find that brighter optical meteors result in radio trains that remain visible for longer, as shown in Figure 3a.

The detected radio emission is integrated over a 2-second time interval. Based on the decay of brightness in subsequent 2-s intervals, the short trails are mostly emission from the meteor's persistent train, rather than from the meteor itself.

The optical trails of CAMS detected meteors start and end at higher altitudes for brighter meteors, and while the radio trains show a similar dependency (Figure 3b and c), the radio emission is first detected at lower altitudes ($h = 101 \pm 4$ km) compared to optical emission ($h = 107 \pm 6$ km). The altitude at which the optical and radio emission ends is comparable for optical ($h = 94 \pm 6$ km) and radio ($h = 92 \pm 6$ km).

Some of the radio trains that were persistent for several minutes were distorted by high altitude winds, much like optical persistent trains. Figure 4 shows an example of the spatial evolution of the radio train with time. The peak intensity of the radio meteor train decreased over time.

Some frequency channels show reflected narrowband artificial radio sources, but all channels contain a broadband radio component that is not likely from artificial radio sources. For bright radio meteors, the signal-to-noise ratio was sufficient to detect this broadband emission in almost all individual channels for frequencies below ∼ 50 MHz. An example is shown in Figure 4.

Further insight was obtained when repeating the AARTFAAC observations during the 2020 Geminid meteor and the 2021 Quadrantid meteor shower. Unfortunately, cloudy weather prevented simultaneous CAMS video observations. During that campaign, the all-sky radio images showed significantly fewer radio meteors compared to the observations of the Perseids.

4 Discussion

We can exclude an important contribution from forward scattered narrow band terrestrial radio emission, which is frequency resolved in our observations. Broadband emission would require a source of very broad band (30–50 MHz) terrestrial radio emission, which we consider unlikely.

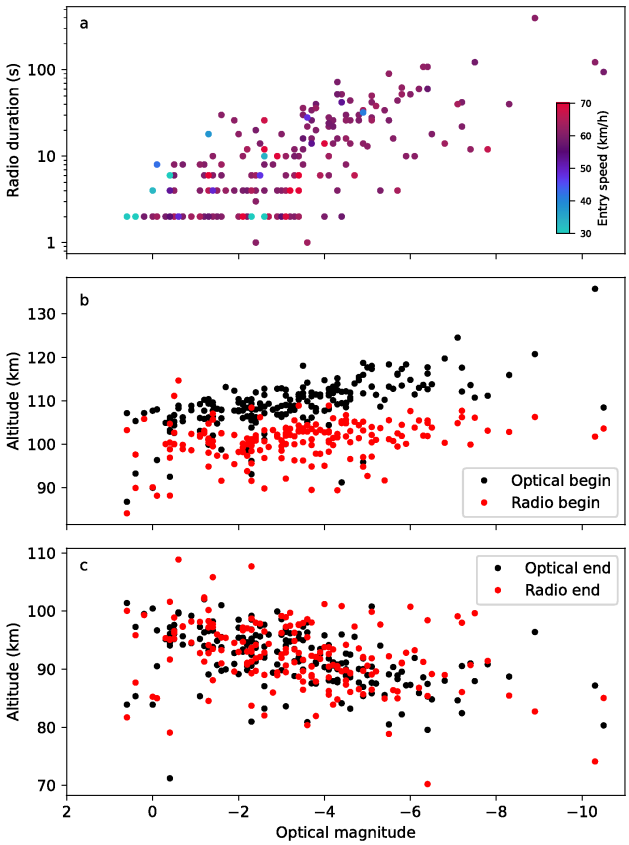

Figure 3 – The dependency of the radio visibility and the altitude of the beginning and end of the meteor trail with optical brightness and entry speed. Note that the CAMS-derived peak optical brightness is less reliable below −5 magnitude due to video blooming.

Of the proposed intrinsic emission scenarios, chemically produced suprathermal electrons (Obenberger et al., 2020) could cause lingering radiation over minutes timescale if those electrons are captured by atoms and molecules that slowly diffuse into the train. Other proposed mechanisms such as Langmuir waves (Obenberger et al., 2015), free-free emission (Filonenko, 2018) and transition radiation (Obenberger et al., 2020), would be expected strong in the meteor itself, but we see the radiation increase in intensity following the meteor head before fading.

There are several possible reasons why fewer meteor trails were detected during the Geminids and Quadrantids. Geminids and Quadrantids are known to reach peak brightness at lower altitudes than the Perseids and show generally weaker optical persistent trains (Jenniskens, 2006). In our case, the lower entry velocities of the Geminids and Quadrantids in comparison to the Perseids is perhaps not to blame. We note that several slower sporadic meteors of similar brightness were observed in radio during the Perseids meteor shower, see Figure 3a.

The atmospheric conditions may be important. During the Perseids, the summer weather provided hot and dry conditions, while the Geminids and Quadrantids were observed during the rainy winter season.

Finally, it is possible that the local sidereal time was important. The scattering of bright celestial radio

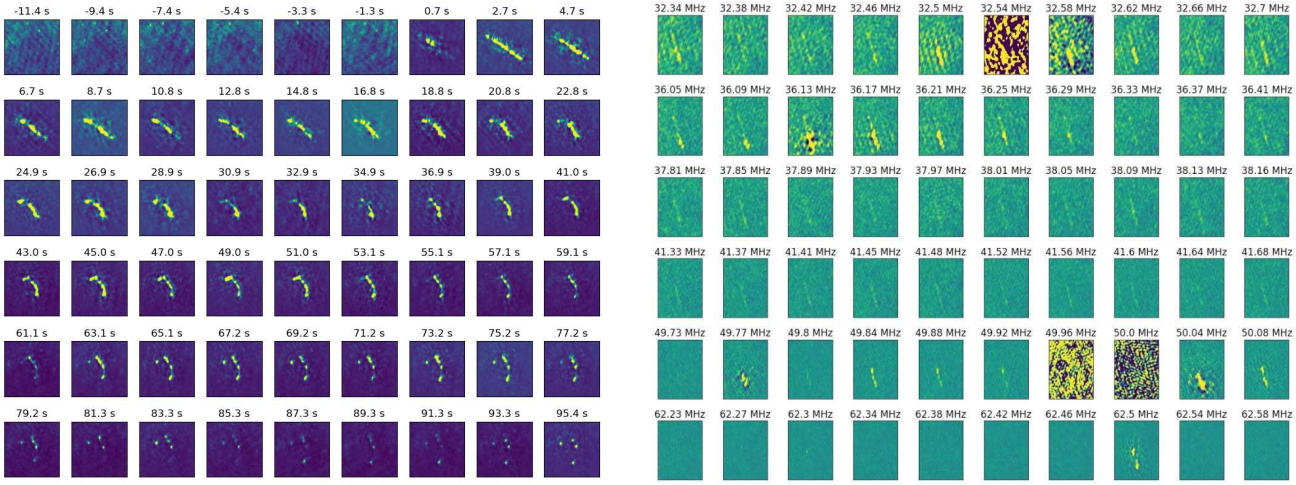

Figure 4 – (Left:) The temporal and spatial evolution of a persistent radio meteor train, showing distortion by high altitude winds. The time is referenced to the beginning of the optical meteor trail. (Right:) Frequency evolution of a meteor train from a bright optical meteor. In channels where the emission from the meteor was very bright, the calibration has failed. That is the case in the bands where narrow-band terrestrial radio emission is reflected from the ionization train. Known transmitters operate at 32.54 MHz (TV transmitter), 49.97 and 49.99 MHz (reflection of the BRAMS meteor radars; Lamy et al. (2016)) and 50.00 MHz (amateur radio transmissions).

sources, as suggested in Obenberger et al. (2015) was rejected in that paper with an argument involving the fact the earlier LWA detections are very bright. Since we have detected much weaker radio meteors, that argument does not hold here.

During the Perseids, the Galactic center and Galactic plane, which is the source of most low-frequency radio emission, was above the LOFAR horizon, while this was not the case during the Geminids and Quadrantids.

5 Conclusions

The AARTFAAC observations presented here show that persistent radio emission from meteors coincides with their optical trajectories, and can be detected for meteors of magnitude ~ 0 and brighter. Aside from a narrow-band scattering of artificial radio sources, there is also a generally broadband emission detected for frequencies below 50 MHz. The continuum radio emission is first detected at lower altitudes compared to the optical emission, while both radio and optical emission end at similar altitudes. For the brightest optical meteors, we find that the radio emission can persist for several minutes. Persistent radio trains are affected by high altitude winds like the optical persistent trains.

Analysis of the AARTFAAC observations is ongoing, so it is currently not possible to distinguish between the suggested origins of the broadband radio emission.

Acknowledgements

We thank Albert van Duin and Edwin van Dijk for the use of facilities at the Edgar Getreuer Observatory in Burlage. We acknowledge interesting discussions with the researchers in the BRAMS project. We thank all camera operators and other contributors to CAMS-BeNeLux. PJ acknowledges support from NASA grant 80NSSC19K0563 (Solar System Workings).

Supplemental materials

Properties of the radio meteors observed simultaneously with CAMS are available as (Dijkema et al., 2021a).

References

Dijkema T. J., Bassa C., Kuiack M., Jenniskens P., Johannink C., Wijers R., and Fallows R. (2021a). "Annotated data of simultaneous broadband radio and optical emission of meteor trains imaged by LOFAR / AARTFAAC and CAMS". Zenodo. https://doi.org/10.5281/zenodo.5644202.

Dijkema T. J., Bassa C., Kuiack M., Jenniskens P., Wijers R., and Fallows R. (2021b). "Time-lapse of AARTFAAC detections of radio meteors in Perseids 2020". Zenodo. https://doi.org/10.5281/zenodo.5595288.

Filonenko A. D. (2018). "High-Frequency Radio Emission from Meteors". *Geomagnetism and Aeronomy*, **58:5**, 693–699.

Jenniskens P. (2006). *Meteor Showers and their Parent Comets*. Cambridge University Press, Cambridge, UK, 790 pages.

Jenniskens P., Gural P. S., Dynneson L., Grigsby B. J., Newman K. E., Borden M., Koop M., and Holman D. (2011). "CAMS: Cameras for Allsky Meteor Surveillance to establish minor meteor showers". *Icarus*, **216:1**, 40–61.

Kuiack M., Huizinga F., Molenaar G., Prasad P., Rowlinson A., and Wijers R. A. M. J. (2019). "AARTFAAC flux density calibration and Northern hemisphere catalogue at 60 MHz". *MNRAS*, **482:2**, 2502–2514.

Kuiack M., Wijers R. A. M. J., Shulevski A., Rowlinson A., Huizinga F., Molenaar G., and Prasad P. (2021). "The AARTFAAC 60 MHz transients survey". *MNRAS*, **505:2**, 2966–2974.

Lamy H., Ranvier S., Anciaux M., Gamby E., Calders S., Tétard C., and De Keyser J. (2016). "BRAMS: a new facility to characterize meteoroids and their interactions with Earth's atmosphere.". In *EGU General Assembly Conference Abstracts*, EGU General Assembly Conference Abstracts. pages EPSC2016–11624.

Lamy H., Ranvier S., de Keyser J., Calders S., Gamby E., and Verbeeck C. (2011). "BRAMS: the Belgian RAdio Meteor Stations". In Cooke W. J., Moser D. E., Hardin B. F., and Janches D., editors, *Meteoroids: The smallest solar system bodies. Proceedings of the Meteoroid Conference held in Breckenridge, Co, USA, May 24-28, 2010*. pages 551–356.

Obenberger K., Taylor G. B., and Holmes J. M. (2016a). "Meteor detections using the LWA". In *AGU Fall Meeting Abstracts*. pages P33E–06.

Obenberger K. S., Dowell J. D., Hancock P. J., Holmes J. M., Pedersen T. R., Schinzel F. K., and Taylor G. B. (2016b). "Rates, flux densities, and spectral indices of meteor radio afterglows". *Journal of Geophysical Research (Space Physics)*, **121:7**, 6808–6817.

Obenberger K. S., Holmes J. M., Ard S. G., Dowell J., Shuman N. S., Taylor G. B., Varghese S. S., and Viggiano A. A. (2020). "Association Between Meteor Radio Afterglows and Optical Persistent Trains". *Journal of Geophysical Research (Space Physics)*, **125:9**, e28053.

Obenberger K. S., Taylor G. B., Hartman J. M., Dowell J., Ellingson S. W., Helmboldt J. F., Henning P. A., Kavic M., Schinzel F. K., Simonetti J. H., Stovall K., and Wilson T. L. (2014). "Detection of Radio Emission from Fireballs". *ApJ*, **788:2**, L26.

Obenberger K. S., Taylor G. B., Lin C. S., Dowell J., Schinzel F. K., and Stovall K. (2015). "Dynamic radio spectra from two fireballs". *Journal of Geophysical Research (Space Physics)*, **120:11**, 9916–9928.

Prasad P., Huizinga F., Kooistra E., van der Schuur D., Gunst A., Romein J., Kuiack M., Molenaar G., Rowlinson A., Swinbank J. D., and Wijers R. A. M. J. (2016). "The AARTFAAC All-Sky Monitor: System Design and Implementation". *Journal of Astronomical Instrumentation*, **5:4**, 1641008.

Prentice J. P. M., Lovell A. C. B., and Banwell C. J. (1947). "Radio echo observations of meteors". *MNRAS*, **107**, 155.

Price C. and Blum M. (2000). "ELF/VLF radiation produced by the 1999 Leonid meteors". *Earth, Moon Planets*, **82-83**, 545–554.

Roggemans P. (2020). "August 2020 report CAMS BeNeLux". *eMeteorNews*, **5:6**, 400–401.

Shulevski A., Franzen T. M. O., Williams W. L., Vernstrom T., Gehlot B. K., Kuiack M., and Wijers R. A. M. J. (2021). "Characterization of the AARTFAAC-12 aperture array: radio source counts at 42 and 61 MHz". *arXiv e-prints*, page arXiv:2103.15160.

van Haarlem M. P., Wise M. W., Gunst A. W., Heald G., McKean J. P., Hessels J. W. T., de Bruyn A. G., Nijboer R., Swinbank J., Fallows R., et al. (2013). "LOFAR: The LOw-Frequency ARray". *A&A*, **556**, A2.

Zhang X., Hancock P., Devillepoix H. A. R., Wayth R. B., Beardsley A., Crosse B., Emrich D., Franzen T. M. O., Gaensler B. M., Horsley L., et al. (2018). "Limits on radio emission from meteors using the MWA". *Monthly Notices of the RAS*, **477:4**, 5167–5176.

Handling Editors: Cis Verbeeck
This paper has been typeset from a LaTeX file prepared by the authors.

Meteorix camera tests for space-based meteor observations

N. Rambaux[1], *J. Vaubaillon*[1], *S. Derelle*[2], *M. Jacquart*[2], *M. Millet*[3], *L. Lacassagne*[3], *A. Petreto*[3], *P. Simoneau*[2], *K. Baillié*[1], *J. Desmars*[1], *D. Galayko*[3], *R. Chotin*[3]

Meteorix is a Universitary CubeSat dedicated to be a demonstrator for the detection and characterisation of meteors and space debris. Its payload is an onboard camera and detection chain. Usually, cameras on CubeSat are used for daylight observations and this proceeding present some tests realized with a sensitive CMOS camera, which is also used in the martian rovers for imaging purposes. In-lab tests were conducted to measure the spectral response. First on-sky images were performed during the 2020 Geminids meteor shower from the Paris area. Follow-up tests were performed from Observatoire de Haute-Provence during the 2021 η-Aquariids meteor shower. Capabilities and needed modifications for meteor detection were identified.

Received 2021 October 12

This work has been presented at the International Meteor Conference 2021 (held online).

1 Introduction

The flux of extraterrestrial material and space debris is not yet determined with great accuracy (e.g. Zolensky et al., 2006; Rendtel & Arlt, 2014; Koschny et al., 2015). To detect meteors, and especially fireballs, large Earth-based networks are set up such as CAMS (Jenniskens et al., 2011), CILBO (Koschny et al., 2013), FRIPON (Colas et al., 2020), DFN (Devillepoix et al., 2020) or the Global Meteor Network (Vida et al., 2020).

Alternatively, mobile stations can be used to observe irregular meteor showers, such as the new 15P-Finlay shower predicted by Vaubaillon et al. (2020) and observed from Chile with MoMET (Da Fonseca et al., 2021). Complementary to these networks, space projects are beginning to emerge, including nanosatellites with the advent of Newspace, to propose meteor science missions (Ishimaru et al., 2014; Rambaux et al., 2019; Petri & Klinkner, 2020). These missions allow to overcome meteorological constraints, to cover a large sky area with a single camera and to detect meteors without the attenuation of the spectrum by the terrestrial atmosphere. Newspace also allows universities to participate in this adventure by directly involving students in these ambitious projects.

The meteor observations from space has been realised by the Meteor experiment onboard of the International Space Station (ISS) allowing to record several sequences of the meteors (Arai et al., 2018). Recently, the Chinese satellite Yangwang has also detected meteors from space.

More specifically, a few nanosatellite projects dedicated to meteor observations are currently developed in the world such as SOURCE at Stuttgart University (Petri & Klinkner, 2020) and Meteorix at Sorbonne Université and associated laboratories (Rambaux et al., 2019). The purpose of this work is to describe the advancement of the optical part of the payload. The detection chain is described in the complementary proceeding (Millet et al., 2021).

2 Meteorix mission

Meteorix is a 3U Universitary demonstrator CubeSat dedicated to the detection and characterisation of meteors and space debris. The main objective is to obtain a robust statistic on the entry of meteoroids and space debris into the Earth's atmosphere. These estimates allow to quantify the flux of extraterrestrial material falling on Earth and to study the interactions of high-velocity meteoroids with the atmosphere as well as the risk of collisions with artificial satellites during meteor showers. The knowledge of the space debris flux will bring an additional constraint for the space awareness models developed in the space agencies. The secondary objectives of this mission are to provide information on the ablation, fragmentation and rotation processes of these objects by measuring the photometric variations of the meteors. In addition, the trajectory of the meteoroids and their dynamical origin will be obtained precisely by combining the detections with those obtained on the ground thanks to the monitoring networks such as FRIPON (Fireball Recovery and InterPlanetary Observation Network) developed in France and which now extends to Europe (Chen et al., 2020). The technological objective of the mission is the demonstration of the feasibility of a real-time computer vision application on board a CubeSat with strong constraints in terms of power consumption and execution time (see Millet et al., 2021).

Finally, this project developed at Sorbonne Université has an important pedagogical dimension by directly involving students in the definition, design, and realisation of the nanosatellite. The scientific and technological objectives fit perfectly in the standard of a small space mission of CubeSat 3 Units developed by students. The project validated the mission definition phase in September 2015 and its feasibility phase in September 2017.

The payload is composed of a visible camera and a detection chain (Rambaux et al., 2019). The obser-

[1]IMCCE, Observatoire de Paris, CNRS, PSL Research University, Sorbonne Université,
Université de Lille, 77 av. Denfert-Rochereau, 75014 Paris, France.
[2]DOTA, ONERA, Université Paris-Saclay, 91123 Palaiseau, France.
[3]LIP6, Sorbonne Université, CNRS, Paris, France.

IMO bibcode WGN-495-rambaux-meteorix
NASA-ADS bibcode 2021JIMO...49..142R

vation is made on the night side of the Earth and the satellite points to the nadir. The nominal life-time of the mission is one year in order to observe the sporadic meteors and to record the main meteor showers. The orbit of the nanosatellite is planned at 500 km altitude on a sun-synchronous orbit.

The design of the CubeSat is based on the CNES cubesat EyeSat (Apper et al., 2020). The bus of the spacecraft is composed of four deployable solar panels in order to increase the energy available on-board and an S-band transmitter for scientific data plus a UHF/VHF transceiver. In addition, the spacecraft has all vital subsystems, a power board, thermal system, a magnetorquer board, one reaction wheel, and on-board computer (see Rambaux et al., 2019).

3 Camera payload

The payload of Meteorix consists in two parts: a camera in the visible domain and an on-board detection chain. The camera is used to record the meteors under the satellite and it is composed of a detector and an optic. The meteors are observed on the night side of the Earth and their detection requires a high sensitivity detector. An off-the-shelf camera is not an optimal solution because most of the Earth CubeSat cameras are dedicated to recorded images during the day. The choice is currently made on the detector 3DCM734 detector of 3Dplus that allows to reach a high enough sensitivity with a quantum efficiency close to 60%. Such detector has a high space-heritage because it flew with the Mars Science Laboratory (Maurice et al., 2021) and on the CNES CubeSat EyeSat (Apper et al., 2020).

A first test phase consisted in verifying the spectral response of the detector. Figure 1 shows the result of a laboratory test campaign of the detector response without optics. This Figure shows the very good agreement between specifications and measurements, confirming the good sensitivity of the detector.

The choice of the optics is not yet confirmed. It has to correspond to the scientific requirements of the detection of a hundred meteors per year requiring a field of view of at least 40 deg (Rambaux et al., 2019).

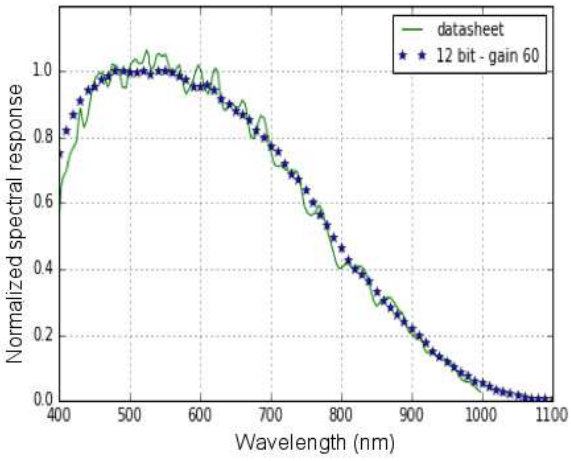

Figure 1 – In-lab measurement of the normalized spectral response of the CMOS monochrome detector 3DCM734 (blue points) compared to manufacturer's data (green curve).

There are commercially available optics with a 6-mm focal length and a 1.4 aperture giving large field of view. Such optics have to be reworked to be compatible with the space environment.

A test campaign was carried out during the meteor shower of η-Aquariids in May 2021. The Figure 2 shows a sequence of a meteor built on image difference. The integration time is 100 ms, the lens used is 6 mm $f/1.4$. The images in the analysis are centered on the meteor so the real field-of-view was larger than displayed here.

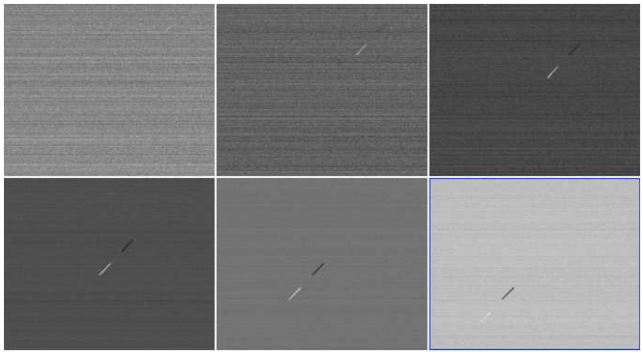

Figure 2 – Sequence of meteor images acquired at the Observatoire de Haute-Provence during the 2021 η-Aquariids with the 3DCM734 detector. The images are differences in order to highlight the meteor. The integration time is 100 ms with cadence of 100 ms.

4 Discussion

These first tests on the selected detector allow to validate its very good sensitivity but two limitations appeared during this phase test. First, the data flow of the full-images (2048×2048) of the detector is limited to a rate of 7 fps due to the use of a space-wire used to communicate with the detector. This data rate is lower than the 10–30 fps required for meteor science objectives and the detection chain algorithms. The current mitigation is to reduce the size of the image (512×512) allowing to accelerate the transfer. A second way of mitigation will be to access directly to the detector registers. Secondly, the detector is used at its sensitivity limit and horizontal lines appear differently for each image. The improvement of these lines is still on working and a back pixel column will be used to clean up the images. In addition, the astrometry of the meteor and the photometry reduction are still in progress.

5 Conclusion

The Meteorix mission is a demonstrator CubeSat mission dedicated to the meteor and space debris science and with technological objectives on the innovative detection chain on-board. This project is developed in laboratories and at the Sorbonne University implying a large number of students that developed new skills around development of a space mission. So this mission is a great source of motivation and inspiration for young people, as the meteor science is challenging and fascinating domain. Currently, the project focused on the payload and the detector has been tested in laboratory and on the ground. The sensitivity of the detector

is confirmed and limitations have been identified. The development of a prototype with a full test-bed meteor simulations and detection chain is on progress.

Acknowledgements

The project acknowledges the ESEP (Exploration Spatiale des Environnements Planétaires), DIM ACAV+ and RFSI Région Île-de-France, CNES Nanolab Academy, and IDEX Sorbonne Universités for funding this research.

References

Apper F., Ressouche A., Humeau N., Vuillemin M., Crooks G., Vindry G., Viaud F., Verdier N., et al. (2020). "EyeSat: a great student adventure within the French space agency leading up to lessons learned from orbit". In *34th SmallSat Conference, 2020*.

Arai T., Kobayashi M., Yamada M., Senshu H., Maeda K., Wada K., Ohno S., Ishibashi K., et al. (2018). "On-Going Status of METEOR Project Onboard the International Space Station". In *49th Lunar and Planetary Science Conference*. Lunar and Planetary Inst., page 2525.

Chen H., Rambaux N., and Vaubaillon J. (2020). "Accuracy of meteor positioning from space- and ground-based observations". *Astronomy and Astrophysics*, **642**, L11.

Colas F., Zanda B., Bouley S., Jeanne S., Malgoyre A., Birlan M., Blanpain C., Gattacceca J., et al. (2020). "FRIPON: a worldwide network to track incoming meteoroids". *Astronomy and Astrophysics*, **644**, A53.

Da Fonseca P., Vaubaillon J., Bouley F., Fasola G., Baillié K., Desmars J., and Amans J.-P. (2021). "Meteorix camera tests for space-based meteor observations". *WGN, Journal of the IMO*, **49:5**, 134–136.

Devillepoix H. A. R., Cupák M., Bland P. A., Sansom E. K., Towner M. C., Howie R. M., Hartig B. A. D., Jansen-Sturgeon T., et al. (2020). "A Global Fireball Observatory". *Planetary and Space Science*, **191**, id. 105036.

Ishimaru R., Sakamoto Y., Kobayashi M., Fujita S., Gonai T., Senshu H., Wada K., Yamada M., , et al. (2014). "CubeSat Mission for UV-Visible Observations of Meteors from Space: S-CUBE (S3: Shootingstar Sensing Satellite)". In *45th Lunar and Planetary Science Conference*. Lunar and Planetary Inst., page 1846.

Jenniskens P., Gural P. S., Dynneson L., Grigsby B. J., Newman K. E., Borden M., Koop M., and Holman D. (2011). "CAMS: Cameras for Allsky Meteor Surveillance to establish minor meteor showers". *Icarus*, **216:1**, 40–61.

Koschny D., Albin T., Drolshagen E., Drolshagen G., Drolshagen S., Koschny J., Kretschmer J., van der Luijt C., , et al. (2015). "Current activities at the ESA/ESTEC Meteor Research Group". In Rault J.-L. and Roggemans P., editors, *International Meteor Conference Mistelbach, Austria*. pages 204–208.

Koschny D., Bettonvil F., Licandro J., Luijt C. v. d., Mc Auliffe J., Smit H., Svedhem H., de Wit F., Witasse O., and Zender J. (2013). "A double-station meteor camera set-up in the Canary Islands - CILBO". *Geoscientific Instrumentation, Methods and Data Systems*, **2:2**, 339–348.

Maurice S., Wiens R. C., Bernardi P., Caïs P., Robinson S., Nelson T., Gasnault O., Reess J. M., , et al. (2021). "The SuperCam Instrument Suite on the Mars 2020 Rover: Science Objectives and Mast-Unit Description". *Space Science Reviews*, **217:3**. id.47.

Millet M., Rambaux N., Petreto A., Lemaitre F., and Lacassagne L. (2021). "Meteorix – a new processing chain for real-time detection and tracking of meteors from space". *WGN, Journal of the IMO*. (submitted).

Petri J. and Klinkner S. (2020). "Stereoscopic meteor observation: Determining satellite bus and formation parameters requirements". In *34th SmallSat Conference, 2020*.

Rambaux N., Vaubaillon J., Lacassagne L., Galayko D., Guignan G., Birlan M., Boisse P., Capderou M., Colas F., Deleflie F., et al. (2019). "Meteorix: A cubesat mission dedicated to the detection of meteors and space debris". In *ESA NEO and Debris Detection Conference - Exploiting Synergies - ESA/ESOC, Darmstadt, Germany*.

Rendtel J. and Arlt R., editors (2014). *Handbook for Meteor Observers*. International Meteor Organization, Potsdam.

Vaubaillon J., Egal A., Desmars J., and Baillié K. (2020). "Meteor shower output caused by comet 15P/Finlay". *WGN, Journal of the IMO*, **48:2**, 29–35.

Vida D., Šegon D., Gural P. S., Brown P. G., McIntyre M. J. M., Dijkema T. J., Pavletić L., Kukić P., et al. (2020). "The Global Meteor Network - Methodology and first results". *Monthly Notices of the Royal Astronomical Society*, **206:4**, 5046–5074.

Zolensky M., Bland P., Brown P., and Halliday I. (2006). "Flux of Extraterrestrial Materials". In Lauretta D. S. and McSween H. Y., editors, *Meteorites and the Early Solar System II*. pages 869–888.

Handling Editor: Ákos Kereszturi
This paper has been typeset from a LaTeX file prepared by the authors.

The International Meteor Organization

www.imo.net

Follow us on Facebook
InternationalMeteorOrganization

Follow us on Twitter
@IMOMeteors

Council

President: Cis Verbeeck,
Bogaertsheide 5, 2560 Kessel, Belgium.
e-mail: cis.verbeeck@scarlet.be

Vice-President: Juraj Tóth,
Fac. Math., Phys. & Inf., Comenius Univ.,
Mlynska dolina, 84248 Bratislava, Slovakia.
e-mail: toth@fmph.uniba.sk

Secretary-General: Robert Lunsford,
14884 Quail Valley Way, El Cajon,
CA 92021-2227, USA. tel. +1 619 755 7791
e-mail: lunro.imo.usa@cox.net

Treasurer: Marc Gyssens, Heerbaan 74,
B-2530 Boechout, Belgium.
e-mail: marc.gyssens@uhasselt.be
BIC: GEBABEBB
IBAN: BE30 0014 7327 5911
Bank transfer costs are always at your expense.

Other Council members:
Javor Kac (see details under WGN)
Detlef Koschny, Zeestraat 46,
NL-2211 XH Noordwijkerhout, Netherlands.
e-mail: detlef.koschny@esa.int
Sirko Molau, Abenstalstraße 13b, D-84072
Seysdorf, Germany. e-mail: sirko@molau.de
Francisco Ocaña Gonzalez, C/ Arquitectura, 7.
28005 Madrid, Spain.
e-mail: francisco.ocana.gonzalez@gmail.com
Vincent Perlerin, 16, rue Georges Bernanos,
51100 Reims, France.
e-mail: vperlerin@gmail.com
Jürgen Rendtel, Eschenweg 16, D-14476
Marquardt, Germany. e-mail: jrendtel@aip.de

Commission Directors

Visual Commission: Jürgen Rendtel
Generic e-mail address: visual@imo.net
Electronic visual report form:
http://www.imo.net/visual/report/electronic
Video Commission: Sirko Molau (video@imo.net)
Photographic Commission: Bill Ward
(bill_meteor@yahoo.com)
Generic e-mail address: photo@imo.net
Radio Commission: Chris Steyaert
(radio@imo.net)
Fireballs: Online fireball reports:
http://fireballs.imo.net

Webmaster

Karl Antier, e-mail: webmaster@imo.net

WGN

Editor-in-chief: Javor Kac
Na Ajdov hrib 24, SI-2310 Slovenska Bistrica,
Slovenia. e-mail: wgn@imo.net;
include METEOR in the e-mail subject line

Editorial board: Ž. Andreić, M. Argo, D.J. Asher,
F. Bettonvil, J. Correira, M. Gyssens,
C. Hergenrother, T. Heywood, J.-L. Rault,
J. Rendtel, C. Verbeeck, S. de Vet, D. Vida.

IMO Sales

Available from the Treasurer or the Electronic Shop on the IMO Website	€	$
IMO membership, including subscription to WGN Vol. 49 (2021)		
Surface mail	26	32
Air Mail (outside Europe only)	49	60
Electronic subscription only	21	25
Proceedings of the International Meteor Conference on paper		
1990, 1991, 1993, 1995, 1996, 1999, 2000, 2002, 2003, per year	9	12
2007, 2010, 2011, per year	15	20
2012, 2013, 2014, 2015 per year	25	34
Proceedings of the Meteor Orbit Determination Workshop 2006	15	20
Radio Meteor School Proceedings 2005	15	20
Handbook for Meteor Observers	15	20
Meteor Shower Workbook	12	16
Electronic media		
Meteor Beliefs Project ZIP archive	6	8

Fireball from Mexico

Sergio Müller captured this beautiful green fireball on the evening of July 7, 2018 from Sonora, Mexico. Notice the fireball passed just to the right of the brilliant planet Mars, which is nearing its closest approach to Earth since 2003. The bright "star" near the top of the frame is actually the planet Saturn. The bright orange star in the right side of the picture is the "heart of the Scorpion" Antares.
Photo courtesy: Sergio Müller.